Structure, petrophysics, and diagenesis of shale entrained along a normal fault at Black Diamond Mines, California—Implications for fault seal

Peter Eichhubl, Peter S. D'Onfro, Atilla Aydin, John Waters, and Douglas K. McCarty

ABSTRACT

The structure, texture, composition, and capillary-pressure resistance were assessed for shale deformed along a normal fault with 9 m (29 ft) of dip separation. Shale is entrained from a 1.6-m (5-ft)-thick source layer into the fault zone and attenuated to about 5 cm (2 in.). A quantitative analysis of shale mineral composition indicates that little material is contributed to the fault rock from the sandstone units that over- and underlie the shale source layer. This finding is in contrast to common predictive models of fault sealing that assume mechanical wear along the fault surfaces. Instead, shale entrainment is inferred to result from incipient distributed shear across a zone of deformation bands in the over- and underlying sandstone, granular flow of the shale, and the increasing localization of deformation in the shale core or along the shale-sandstone interfaces of the evolving fault zone. The composition of deformed shale indicates the effective mixing of clay- and quartz-rich layers of the shaly source unit by granular flow during shale deformation.

Capillary displacement pressures of deformed shale are 30% higher compared to the most clay-rich undeformed shale outside the fault. This increase in sealing capacity, in combination with a 50% anisotropy in capillary displacement pressure, is primarily attributed to the development of a planar fabric in deformed shale. Enhanced clay diagenesis likely contributed to the increase in shale sealing capacity. We conclude that fault seal by shale entrainment involves a variety of structural, textural, and diagenetic processes that require an integrated methodology for improved predictions of fault-sealing capacity.

Manuscript received September 18, 2004; provisional acceptance December 7, 2004; revised manuscript received April 21, 2005; final acceptance April 22, 2005.

DOI:10.1306/04220504099

AUTHORS

PETER EICHHUBL ~ *Department of Geological and Environmental Sciences, Stanford University, Stanford, California 94305; present address: Department of Physical and Life Sciences, Texas A&M University–Corpus Christi, 6300 Ocean Drive, Corpus Christi, Texas 78412; peichhubl@falcon.tamucc.edu*

Peter Eichhubl received his M.S. degree at the University of Vienna, Austria, and his Ph.D. at the University of California, Santa Barbara. After research positions at Stanford University and Monterey Bay Aquarium Research Institute, he joined the faculty at Texas A&M University–Corpus Christi. His research interests include the interaction of chemical mass transfer and brittle deformation, diagenesis, and fault and fracture mechanics.

PETER S. D'ONFRO ~ *ConocoPhillips, P.O. Box 2197, Houston, Texas 77252-2197; donfrps@conocophillips.com*

Peter D'Onfro earned his B.S. and M.S. degrees from Boston College. After a research position at Los Alamos National Laboratories, he joined Conoco in 1979 and then ConocoPhillips in 2002. He specializes in bed and fault-seal analysis for exploration prospect and reservoir performance evaluations.

ATILLA AYDIN ~ *Department of Geological and Environmental Sciences, Stanford University, Stanford, California 94305; aydin@pangea.stanford.edu*

Atilla Aydin received his B.S. degree in geology from the Istanbul Technical University in Turkey and both his M.S. degree and his Ph.D. in geology from Stanford University. He is a research professor of structural geology and geomechanics and codirector of the Rock Fracture Project at Stanford University. His research interest includes fracturing and faulting of rocks and fluid flow in fractured and faulted rocks and regions, with application to hydrocarbon migration, entrapment, and recovery.

JOHN WATERS ~ *Black Diamond Mines Regional Preserve, Antioch, California 94509; jwaters@ebparks.org*

John Waters directs abandoned mine reclamation and development for the East Bay Regional Park District, a San Francisco Bay area

park agency. His responsibilities include the development of an abandoned underground mine for use as a museum and a site for geotechnical research and education. John also serves as a consultant to other agencies and private industry on abandoned-mine–related issues.

DOUGLAS K. MCCARTY ~ *ChevronTexaco, 3901 Briarpark, Houston, Texas 77042; DMcCarty@chevrontexaco.com*

Douglas McCarty received his B.S. and M.S. degrees at the University of Montana and his Ph.D. in geology at Dartmouth, with a specialty in clay mineralogy. After a research position at Montana State University, he started work at what is now ChevronTexaco in 1997. His research interests relate to mineralogy and its geological relationships.

ACKNOWLEDGEMENTS

We thank Ray Sullivan for insightful discussions on the Domengine depositional environment and for providing an expanded stratigraphic section. Park ranger Pat Dedmon provided assistance during sample collection and fault excavation. The personnel of the Black Diamond Mines Regional Preserve are thanked for general logistic support. The manuscript benefited from reviews by *AAPG Bulletin* reviewers Stephen Dee, Ted Doughty, and Ron Nelson. This study was supported by the industrial affiliates of the Stanford Shale Smear Project, with laboratory analyses and printing costs paid for by ConocoPhillips.

INTRODUCTION

The entrainment of shale along faults in sandstone-shale sequences, commonly referred to as shale smear, potentially impedes the flow of hydrocarbons and water across fault contacts that juxtapose sandstone against sandstone (Smith, 1980; Lindsay et al., 1993; Knipe et al., 1997). Such faults may form economic hydrocarbon traps depending on the petrophysical properties of the entrained and deformed shale and its extent and continuity along the fault surface. The effect of shale on impeding fluid flow is attributed to two processes commonly referred to as membrane or static sealing and hydraulic-resistance or dynamic sealing (Watts, 1987; Heum, 1996; Brown, 2003). Membrane-sealing behavior results from the capillary pressure that resists flow of the nonwetting fluid phase in a two- or multiphase system across necks in the continuous pore system of the shale (Watts, 1987). The size of the trap is, in this case, controlled by the hydrocarbon-column height that the seal can support because of its capillary-pressure resistance for flow of the nonwetting hydrocarbon phase. Hydraulic-resistance sealing is controlled by the matrix or fracture permeability of the shale, which is applicable to single- and multiphase fluid systems. The size of a trap formed by a hydraulic-resistance seal is controlled by the rate of reservoir charge relative to the leakage rate. Although the sealing behavior of any given faults may vary with depth, lithologic juxtaposition, and reservoir and fault fluid composition (Brown, 2003; Bretan et al., 2003), trap size in many hydrocarbon systems is believed to be controlled by membrane-sealing behavior (Schowalter, 1979). The prediction of fault properties that control the membrane-sealing behavior is thus of fundamental importance for predicting oil and gas in place in hydrocarbon exploration.

Seal prediction of faults containing entrained shale has thus focused on two controlling factors: (1) the geometric properties of the shale layer and (2) the petrophysical properties that determine the sealing capacity of the shale. Studies on the geometric properties have largely addressed the shale continuity as a function of shale composition, slip distance, and structural style (Weber et al., 1978; Smith, 1980; Bouvier et al., 1989; Lindsay et al., 1993; Gibson, 1994; Childs et al., 1997; Lehner and Pilaar, 1997; Yielding et al., 1997; Koledoye et al., 2000, 2003; Younes and Aydin, 2001; Aydin and Eyal, 2002; Doughty, 2003). Current models predicting the sealing capacity of shale in faults are based on reservoir calibrations of measured pressure differentials across faults, with a single parameter that relates to fault rock composition (Yielding et al., 1997; Skerlec, 1999; Harris et al., 2002; Yielding, 2002). This parameter, referred to as the shale gouge ratio by Yielding et al. (1997, p. 900–901), relates to the volume fraction of clay minerals or phyllosilicates integrated over the thickness of shale and sand units that have slipped past a point on the fault over the finite slip distance. The shale gouge ratio is considered to equal the volume fraction of clay minerals of the entrained shale assuming perfect mixing of clay and nonclay minerals and an equal contribution of

shale and sand from the host rock to the fault. This parameter is then empirically calibrated to pressure differentials across faults in the same field.

The ability of the shale gouge ratio and similar single-parameter criteria to sufficiently characterize the shale-sealing capacity appears, based on our review of published analyses, uncertain. A comparison of clay mineral content of fault rock with measured mercury intrusion experiments by Gibson (1998) suggests that clay mineral content may provide an upper limit of predicted pore-throat radii and, thus, on minimum membrane-sealing capacity but no constraint on maximum sealing capacity; nor does the clay mineral content of naturally deformed shale appear well correlated with a simple mixing law such as the shale gouge ratio. For instance, the published data set (Yielding, 2002) that provides the basis for the shale gouge ratio of Yielding et al. (1997) shows a moderate correlation ($R^2 = 0.71$) between measured and predicted clay mineral content of fault rock, with 20% of their measured values deviating from the predicted value by 20–30%.

This study was designed to assess the sealing capacity of a naturally deformed shale relative to the undeformed shale to test some of the fundamental assumptions behind these single-parameter seal capacity models. Based on a detailed compositional analysis of the deformed shale, in conjunction with laboratory capillary-pressure measurements, we shall demonstrate that, at least in this particular case study, fault-sealing capacity is severely underestimated by a simple mixing law. Instead, we propose that successful fault-seal prediction in shale-sandstone sequences has to consider the structure of the fault zone, the dominant deformation mechanism and the resulting internal structure of the deformed shale, as well as the depositional and diagenetic aspects of shale composition.

Following common usage in petroleum geology, the term ''shale'' is used in this study in a wider sense to include laminated and nonlaminated, fine-grained detrital rock synonymous with mudrock of Ingram (1953), thus including silt- and clay-size grains (Pettijohn, 1975). Clay refers to grains less than 2 μm, and clay mineral represents a species of a group of phyllosilicates (Bailey, 1980) irrespective of grain size.

GEOLOGIC SETTING

This study analyzed naturally deformed shale from a normal fault that is exposed in a historic quartz sand mine, the Hazel-Atlas Mine located in the Black Diamond Mines Regional Preserve, Antioch, California (Sullivan and Waters, 1980; Sullivan et al., 1994, 2003). This underground setting was chosen to minimize the effects of surface alteration on shale composition and petrophysical properties while permitting access for controlled sampling and structural observations. The fault, referred to as the Hazel-Atlas fault by Sullivan et al. (2003), offsets a sandstone-shale sequence that is part of the 230–260-m (754–853-ft)-thick Domengine Formation of middle Eocene age (Sullivan et al., 1994, 2003). The 185-m (606-ft)-thick lower member of this formation is composed of cross-bedded estuarine subtidal sandstone that is interbedded with bioturbated intertidal mudrock and supratidal coal layers (Figure 1). Three distinct coal-bearing mudrock layers in the lower member of the Domengine Formation are referred to as, from bottom to top, the Black Diamond, Little, and Clark veins (Goodyear, 1877), of which only the Clark vein is exposed in the currently accessible parts of the mine workings (Figure 1). The use of the term ''vein'' in these names follows the miner's tradition to refer to a mineralized layer without implying epigenesis. These up to 5-m (16-ft)-thick layers are composed of carbonaceous mudstone with interbedded sand laminae and layers of subbituminous coal (Cooper et al., 1947; Davis and Goldman, 1958) that were mined during the 19th century (Sullivan and Waters, 1980).

The faulted and deformed shale layer investigated in detail for this study is a carbonaceous mudstone layer 14 m (45 ft) below the Clark vein (Figure 2a). This layer, informally referred to as the Sully vein by Sullivan et al. (2003) (Figure 1, this study), has a stratigraphic thickness of 1.6 m (5 ft) in the vicinity of the Hazel-Atlas fault. For the purpose of this study, the Sully vein was subdivided into six subunits based on their outcrop character, referred to, from bottom to top, as layers A to F (Figure 2b). Layers A, C, and E appeared in outcrop more clay rich, and layers B, D, and F appeared in outcrop more sand rich. Layer A is a dark-gray to black, dense mudrock with poorly developed fissility (Figure 3a). Exposure of this shale in the mine tunnel resulted in an about 5-cm (2-in.)-thick weathered layer containing abundant veins that are filled with greenish-blue melanterite ($FeSO_4 \cdot 7H_2O$) and halotrichite ($FeAl_2(SiO_4)_4 \cdot 22H_2O$). This weathered layer was removed for sampling. Layers C and E are composed of black, porous, friable carbonaceous mudrock with subordinate lenses or thin beds of sandstone (Figure 3b). Layers B, D, and F are composed of sand and silt layers alternating with laminae of black

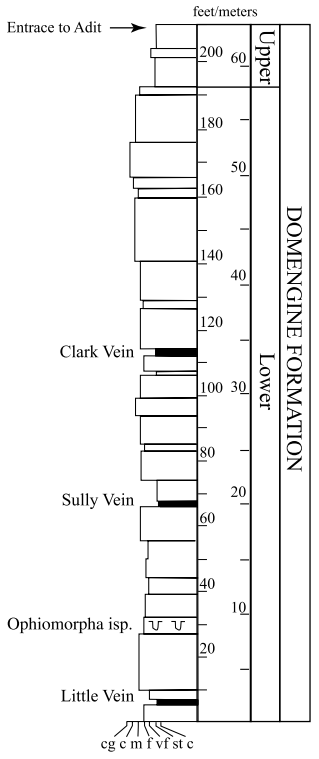

Figure 1. Stratigraphic section across parts of the lower and upper Domengine Formation as exposed in the Greathouse adit of the Hazel-Atlas Mine. Modified after Sullivan et al. (2003); designation of Little vein is based on Goodyear (1877). Grain size abbreviations: cg = conglomerate; c = coarse-grained sand; m = medium-grained sand; f = fine-grained sand; vf = very fine-grained sand; st = silt; c = clay.

carbonaceous mudrock (Figure 3a, b). The Sully vein lacks economic quantities of coal and has not been mined.

Unless noted otherwise, the following description is based on exposures in the B level of the Hazel-Atlas quartz sand mine workings. Where not disturbed by later mining operations, two tunnels follow the strike of the units: a lower haulage drift and, commonly directly above, an upper machinery drift. Considerations of preserving the historic character of this mine limited detailed sampling to exposures in the machinery drift of the B level.

FAULT STRUCTURE

The Hazel-Atlas fault strikes N49°E, dips 68° to the northwest, and displaces the sandstone-shale sequence of strike N108°E, dip 31°N, by a dip separation of 9 m (29 ft) of normal slip (Figure 4). Dip separation was calculated based on the vertical separation of the base of the Sully vein measured to both sides of the fault relative to the surveyed floor of the haulage drift in the B level of the mine. No piercing points are observed that would unambiguously define the magnitude and direction of finite slip. Faint striations on the fault surface with rake of 70° southwest suggest predominant dip slip with a smaller left-lateral strike-slip component and a total finite slip magnitude of 7.6 m (25 ft) (Figure 4, inset).

The machinery drift in the B level exposes the hanging-wall cutoff of the Sully vein (Figure 2a, b) and about 2 m (6.6 ft) of the fault above the hanging-wall cutoff. The footwall cutoff of the Sully vein is not exposed and only shown interpretively in Figure 4. The base of the Sully vein in the footwall is exposed in the ceiling of the machinery drift about 20 m (66 ft) east of the fault, where its elevation has been surveyed with a range finder for the determination of the vertical fault separation. A complete section of the Sully vein is exposed in the footwall section of the fault in a caved-in section of the B level about 180 m (590 ft) east of the fault. The correlation of the Sully vein across the fault and between these exposures is based on the detailed stratigraphy of Sullivan et al. (2003) and using a marker bed with abundant Ophiomorpha burrows 12 m (39 ft) below the Sully vein and the Clark vein 12 m (39 ft) above the Sully vein as reference units (Figure 1).

The shale layer in the hanging wall of the fault as exposed in the machinery drift is characterized by an increasing density of small normal faults within 0.5–1 m (1.6–3.3 ft) of the principal fault contact (Figure 2a, b). These faults are oriented at a high angle to bedding and offset the sandy layers in the Sully vein (Figure 3c). Within 20–40 cm (8–16 in.) of the fault, isolated fragments of the sandy layers become entrained and rotated within clay-rich shale (Figure 3d). These sand-rich fragments have notably diffuse boundaries to the surrounding clay-rich shale. This 20–40-cm (8–16-in.)-thick zone of intense shale deformation and entrainment of sandy layers will be designated as the transition zone for the purpose of this study. This transition zone, corresponding to the juxtaposition of sandstone in the footwall against the shale layer in the hanging wall, will be distinguished from the attenuated shale contained in the fault segment that juxtaposes the sandstone of the footwall against the sandstone in the hanging wall. Shale contained in the transition zone and attenuated shale within the fault will be referred to collectively as deformed shale.

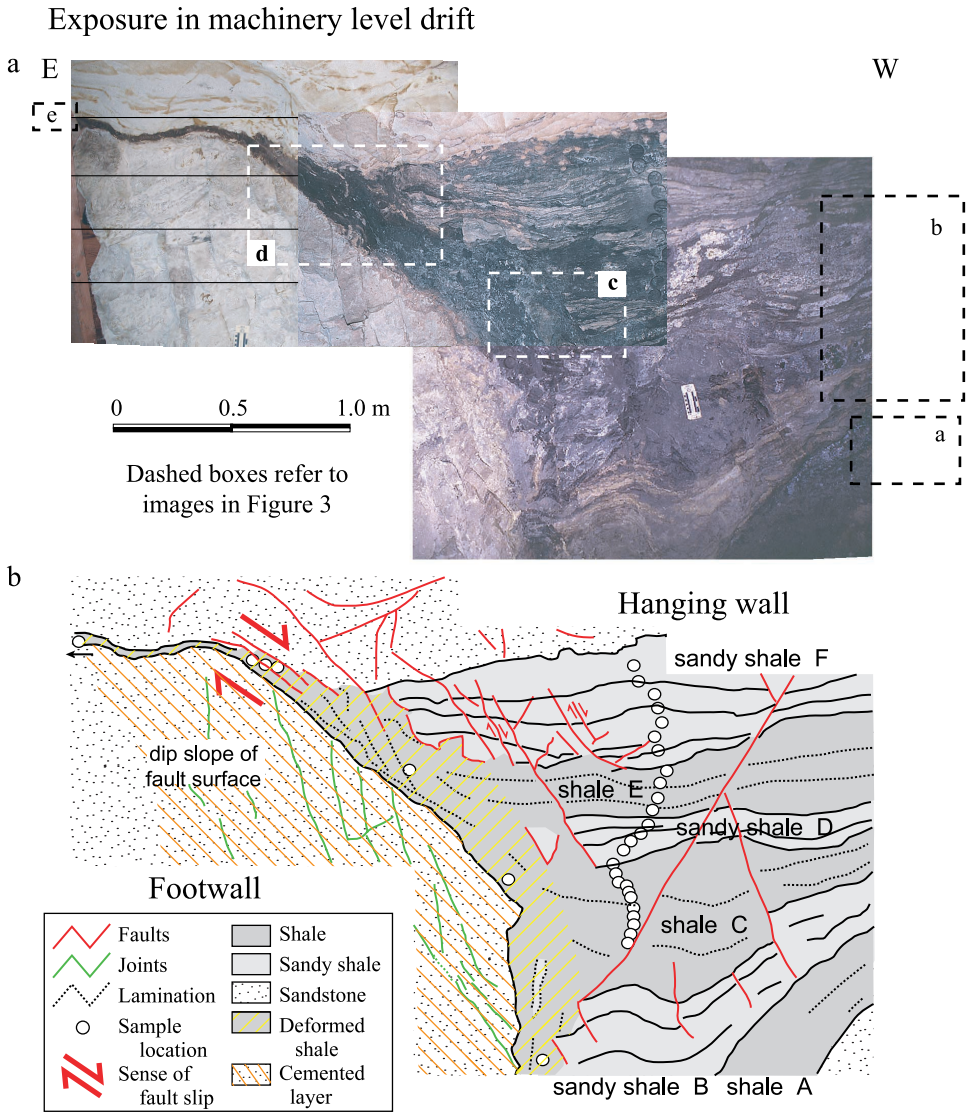

Figure 2. (a) Photomosaic of the hanging-wall cutoff of the Sully vein and the lower portion of attenuated shale along the Hazel-Atlas fault, B level machinery drift. (b) Outcrop structure map based on (a). With increasing proximity to the main fault, sand-rich layers of the shale layer are disrupted by small faults and entrained into the clay-rich shale. (c) Base of Sully vein (layer A) in hanging wall and attenuated shale in the Hazel-Atlas fault below the Sully vein, B level haulage drift. Red arrow points to sand layers interpreted as remnant of depositional layering. Measuring scale is in centimeters. (d) Outcrop sketch of the base of Sully vein and the attenuated shale in the Hazel-Atlas fault below the Sully vein, B level haulage drift.

Within the fault, the deformed shale attenuates to about 5 cm (2 in.) (Figure 3e, f). The shale is reddish brown in color, with the firm but malleable consistency of molding clay although feeling gritty to the touch. Tan-colored sandy portions form laminae and elongate pods with internal stratification (Figure 3e). The long dimension of these pods is oblique to the bounding surfaces of the attenuated shale and synthetic to the sense of slip of the fault (Figure 3f). The laminae of sandy portions in the attenuated shale are in conformable, and apparently depositional, contact with the footwall (Figure 3e). Discrete fault surfaces can be

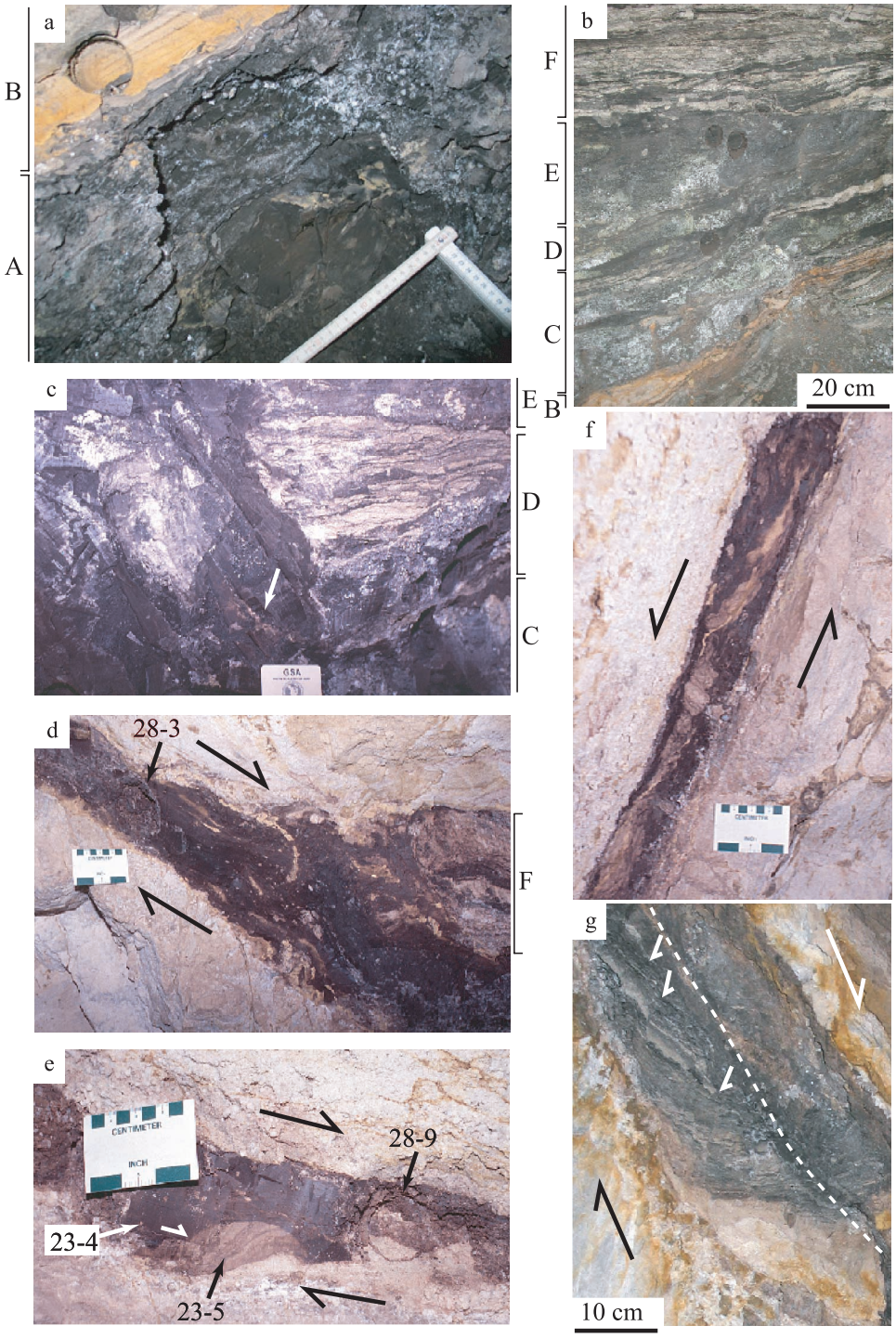

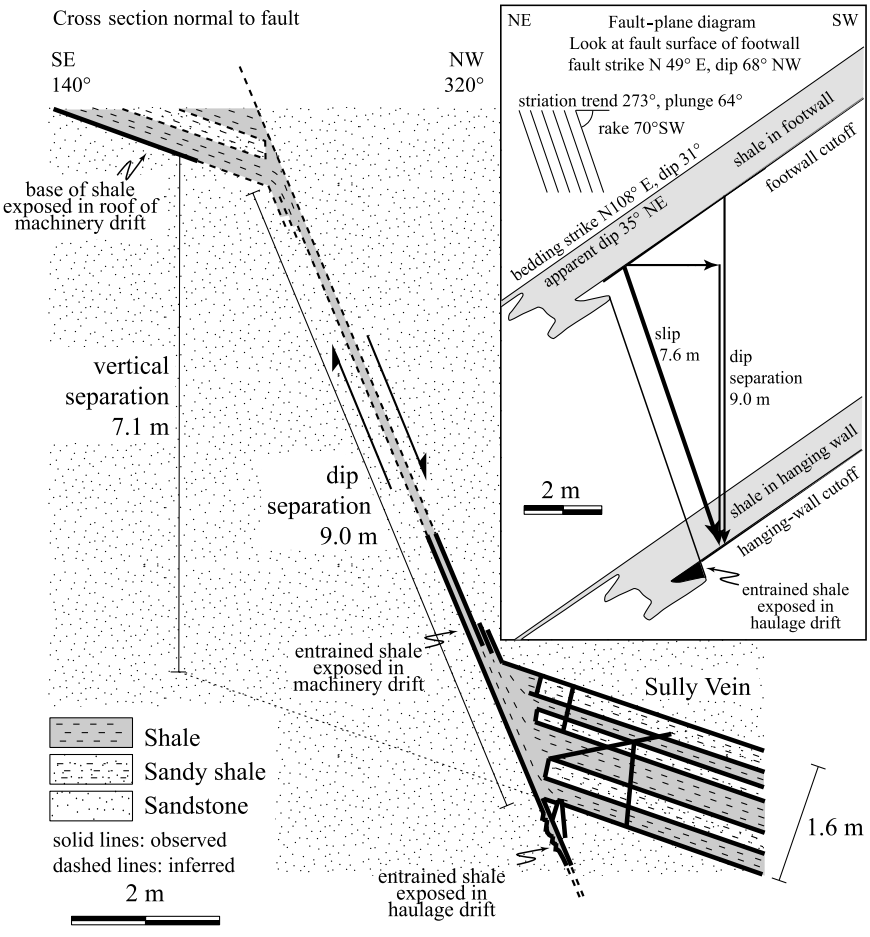

Figure 4. Schematic cross section across the Hazel-Atlas fault perpendicular to the fault surface. Inset: fault-plane diagram for calculation of the finite slip distance on the fault.

distinguished in these sandy, laminated portions, with sense of slip consistent with the overall slip direction on the fault (white half arrow in Figure 3e.).

The sandstone below and above the Sully vein is well sorted, friable by hand, and has locally well-developed Liesegang bands. The sandstone contains abundant deformation bands that, with decreasing distance from the fault, are cemented by an increasing amount of dark clay or oxide minerals that accentuate these bands in outcrop. A 5-cm (2-in.)-thick layer in the footwall

Figure 3. (a–e) Outcrop photographs of the north side of machinery drift. (a) Clay-rich layer A, with weathered oxidation layer removed and base of sandy shale B about 2 m (6.6 ft) away from the fault. Scale in centimeters. (b) Layers B–F (indicated by brackets on the left of the figure) of Sully vein 2 m (6.6 ft) away from the fault. The Sully vein is composed of sand-rich and clay-rich layers. Circular marks indicate sample location 28/4-8. (c) Truncation of the sandy shale layer D. The abrupt termination and the fragment of sandy layer (left half of image) are indicative of brittle deformation of sandy layers, whereas shale is deformed by distributed granular flow. Notice the sand-rich stringer (arrow) within the shale originating from the base of layer D. White areas are covered by a thin coat of oxidation crust. (d) Deformed shale of the transition zone (right) and attenuated shale (left). Notice the sharp termination of sand-rich layers to the right. Sand-rich layers become entrained into the attenuated shale, forming elongate nodules and pods. The location of sample 28-3 is shown by the arrow. Scale in centimeters (7 cm) on top and inches (3 in.) on the bottom. (e) Detail of attenuated shale at sample location 28-9 (circular saw mark) and 23-4 and 23-5. The attenuated shale is composed of dark clay-rich (sample 23-4) and lighter colored laminated quartz-rich layers (sample 23-5) interpreted as a remnant of depositional layering. (f) The attenuated shale composed of dark clay-rich and lighter colored quartz-rich shale. Layers are oriented slightly oblique to the bounding fault surfaces. Picture is from the south side of machinery drift. (g) Attenuated shale along the Hazel-Atlas fault below the Sully vein exposed in the north side of the haulage drift. Laminations in attenuated shale are offset by small faults at high angle to the main fault surface. Dashed line indicates slip surface within deformed shale. See Figure 2d for location of figure.

immediately in contact with the attenuated shale is well cemented, is composed of multiple deformation bands that are parallel to the fault surface, and contains joints perpendicular to the fault (Figure 2a, b).

The B level haulage drift exposes the lowermost section of the hanging-wall transition zone and about 1.5 m (5 ft) of the Hazel-Atlas fault below the Sully vein where the fault contains an 8–15-cm (3–6-in.)-thick layer of attenuated shale (Figures 2c, 3g). Similar to observations on attenuated shale above the Sully vein, attenuated shale below the Sully vein contains laminae of sand and sandy shale (red arrow in Figures 2c, 3g) in contact with the footwall sandstone. Preserved depositional structures in these laminae indicate that the contact between the deformed shale and the footwall sandstone is depositional in origin. This sandstone-shale contact is offset along numerous 2–10-cm (0.8–4-in)-spaced subvertical faults with a synthetic sense of slip relative to the overall sense of slip along the Hazel-Atlas fault (Figures 2d, 3g). Between these subvertical faults, the shale laminae are rotated in the direction of the fault dip, approaching parallelism with the fault in the center of the deformed shale (Figure 3g).The top half of the attenuated shale is more strongly sheared similar to the attenuated shale in the machinery drift, with the depositional layering largely obliterated. The strain in the deformed shale appears localized along a slip surface that is located within, instead of along the bounding surfaces of, the deformed shale (dashed line in Figure 3g).

The stratigraphic correlation of the Sully vein across the Hazel-Atlas fault excludes the Little vein, the next lower shale layer of regional extent approximately 18 m (59 ft) below the Sully vein (Figure 1), as a possible source for the attenuated shale exposed in the B level haulage drift. Instead, we interpret this attenuated shale as derived from a shale body of limited lateral extent below the Sully vein but otherwise not exposed in the B level haulage drift. Alternatively, the apparent structural position of this attenuated shale below the Sully vein could be attributed to lateral changes in layer thickness of the Sully vein and the interfingering of sand and shale as portrayed in Figure 4 (inset). Changes in shale layer thickness over short distances along strike are consistent with the depositional environment of the Domengine Formation (R. Sulllivan, 2004, personal communication). Structures indicative of reverse slip along the fault were not observed, making it unlikely that the entrained shale observed in the haulage level resulted from structural inversion.

SAMPLING AND ANALYTICAL METHODS

Samples of shale and sandy shale were taken from the north side of the B level machinery drift using a drill without water coolant to avoid contamination and after removal of the altered surface layer. The undeformed shale layers were sampled in a continuous array of core plugs at a distance of 1–2 m (3.3–6.6 ft) from the fault (Figure 5). The samples were ground and mixed in the laboratory to provide representative bulk rock samples of layers A–F for quantitative mineral compositional analysis. In addition, oriented samples were collected for textural and petrophysical analysis from each of layers A, C, E, and F (Figure 5). Four samples were taken from the transition zone (Figure 5), and six were taken from the attenuated shale within the fault. Of the three samples taken from the most attenuated part of the fault, sample 23-4 was taken from a darker, presumably more clay-rich, area, and sample 23-5 was taken from a lighter, more sand-rich area (Figure 3e). Sample 28-9 contained both clay-rich and sand-rich layers.

Chips with freshly broken surfaces of these samples were imaged on a JEOL scanning electron microscope (SEM) to image textural changes resulting from faulting. Capillary-pressure measurements were performed by mercury injection at PetroTech Associates (Houston, Texas) following techniques described by Sneider et al. (1997). For select samples, faces perpendicular to the shale fissility of cube-shaped samples about 1 cm^3 (0.06 $in.^3$) in size were coated or jacketed with epoxy to force mercury injection along the direction perpendicular to the fissility. By measuring both jacketed and unjacketed shale samples, it is assumed that the entry or displacement pressures of unjacketed samples measure intrusion parallel to the fissility of the shale (Sneider et al., 1997). Differences between jacketed and unjacketed samples are thus a measure of the textural anisotropy of these samples. Mercury displacement pressures are reported for 7.5% mercury saturation following Sneider et al. (1997), who found that displacement pressures picked at 7.5% mercury saturation correspond best to the heights of hydrocarbon columns measured in many reservoirs. Pore-throat aperture r was calculated using the equation $r = 2\gamma\cos\theta/p_c$ (Berg, 1975) where γ is the interfacial tension, θ is the contact angle between the liquid and the solid, and p_c is the measured injection pressure.

Quantitative x-ray diffraction (QXRD) was conducted on bulk samples following the procedure of Środoń et al. (2001). This technique uses an internal

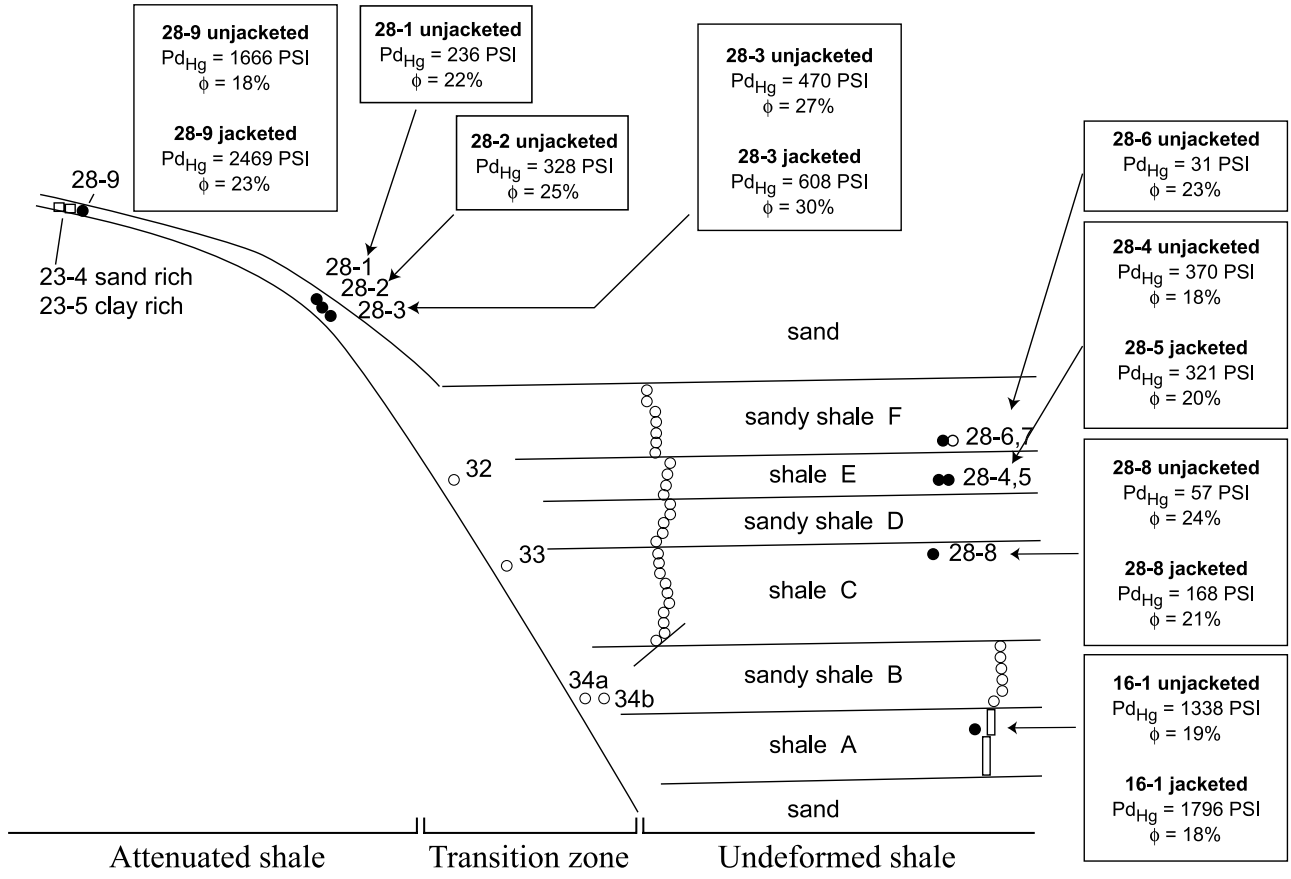

Figure 5. Sample locations on the north side of the B level machinery drift and distribution of mercury displacement pressures Pd_{Hg} and porosity ϕ of shale samples. Filled circles indicate samples analyzed by mercury intrusion and empty circles for compositional and textural analyses.

standard (Chung, 1974) and directly calculates the abundance of individual nonclay mineral phases and of clay mineral families without normalization. The error for typical mudstones is generally less than 2 wt.% from the actual content for each mineral component (Środoń et al., 2001). For oriented aggregate sample analysis of the clay-size fraction, the less than 2-μm equivalent spherical diameter size fraction was separated from samples by standard centrifugation methods. Details of the clay-mineral XRD analysis are given in the Appendix.

Elemental composition of bulk samples was analyzed by Chemex Laboratories (Vancouver) using standard x-ray fluorescence (XRF) for major elements and inductively coupled plasma–mass spectrometry (ICP-MS) for trace elements following dissolution by lithium metaborate fusion. Elemental analysis included volatile content by loss on ignition (LOI) at 1010°C for 1 hr and total carbon content by combustion at 1500°C in a Leco induction furnace coupled with a CO_2 infrared analyzer. The grain size distribution of three samples was measured by laser particle size analysis at Core Laboratories (Houston).

MINERALOGICAL COMPOSITION

Undeformed Shale and Sandstone

The predominant mineral phases in the undeformed shale layer are quartz, kaolinite, potassium feldspar, mixed-layer clays, and illite (Tables 1, 2; Figures 6, 7). Minor mineral components are carbonate minerals, pyrite, and sulfates, including the mineral jarosite ($KFe_3(SO_4)_2(OH)_6$). Mixed-layer clays include randomly interstratified (Reichweite of 0) illite-smectite-vermiculite (I-S-V) and kaolinite-smectite-vermiculite (K-S-V) (Table 2). The term ''vermiculite'' is used here to designate a high-charge smectite layer with less than two layers of water or ethylene glycol molecules in the

Table 1. Summary of Bulk Rock Mineralogical Analyses by X-Ray Diffraction*

Sample	Qtz	Kspar	Plag	Cal	Mg-Cal/ Dol	Py	Sid	Anh	Ank	Gyp	Total Nonclay	Kaol	2:1 Clays	Tri 1:1 Clays	Total Clays
20-1	93	6	0	0	0	0	0	0	0	0	99	1	2	0	3
F	40	20	0	0	1	0	0	0	0	1	63	19	22	0	42
E	30	14	0	0	1	0	0	1	1	0	47	30	18	1	49
D	31	13	1	1	1	1	0	0	1	1	50	29	22	3	53
C	35	18	1	0	1	3	0	0	1	1	59	21	18	4	43
B	40	19	1	0	1	0	0	1	0	1	62	18	22	1	42
A	25	9	0	0	1	7	0	1	1	1	45	28	23	4	55
32	36	16	0	0	1	1	0	0	1	1	56	28	15	3	46
33	34	16	0	1	1	5	1	1	0	1	58	24	19	2	45
34-a	37	18	0	0	1	0	0	1	0	1	57	23	17	1	42
34-b	40	16	0	0	1	0	0	0	0	0	57	21	18	2	41
28-3	36	15	1	0	0	0	1	1	1	1	56	24	15	2	41
23-4	36	14	0	0	1	0	0	0	1	1	53	27	20	5	52
23-5	42	19	0	0	1	1	1	0	0	0	64	25	14	1	40
28-9	39	14	0	0	1	0	1	1	1	1	57	29	13	0	42

*Qtz = quartz; Kspar = potassium feldspar; Plag = plagioclase; Cal = calcite; Mg-Cal/Dol = high-Mg calcite or dolomite; Py = pyrite; Sid = siderite; Anh = anhydrite; Ank = ankerite; Gyp = gypsum; Kaol = kaolinite.

interlayer site in the air-dried or solvated states, respectively. Layer A has the highest clay mineral content with 55%, and layers B and F have the lowest with 40% (Figure 6c). Inversely, layer A has the lowest quartz content of 25%, and layers B and F have the highest with 39 and 38%, respectively (Figure 6a). Note that layer D, which, because of its lighter color, appeared more sand rich in the field compared to layer C, has 5% less quartz than layer C. The mean clay mineral content of layers A–F, weighted to account for the different layer thicknesses, is 47% (WM in Figure 6c). The weighted mean quartz content across layers A–F is 34%

Table 2. Summary of X-Ray Diffraction Mineralogical Analyses of Clay-Size (<2-μm) Fraction

	R_0 I-S-V		R_1 I-S-V		R_0 K-S-V		Smectite	Illite	Kaolinite
Sample	Amt (%)	% S + V	Amt (%)	% S + V	Amt (%)	% S + V	Amt (%)	Amt (%)	Amt (%)
20-1								20	80
F							39	1	60
E	3	70			9	89		4	84
D	9	85			20	95		1	70
C	22	91			14	95		1	63
B							52	1	47
A	8	94			13	80		2	77
32					8	90		4	88
33							23	3	74
34a	5	95			2	90		6	87
34b	10	65			8	19		8	74
28-3	3	80						9	88
23-4			12	60	11	27		4	73
23-5	6	85			14	80		2	78
28-9	5	80						7	88

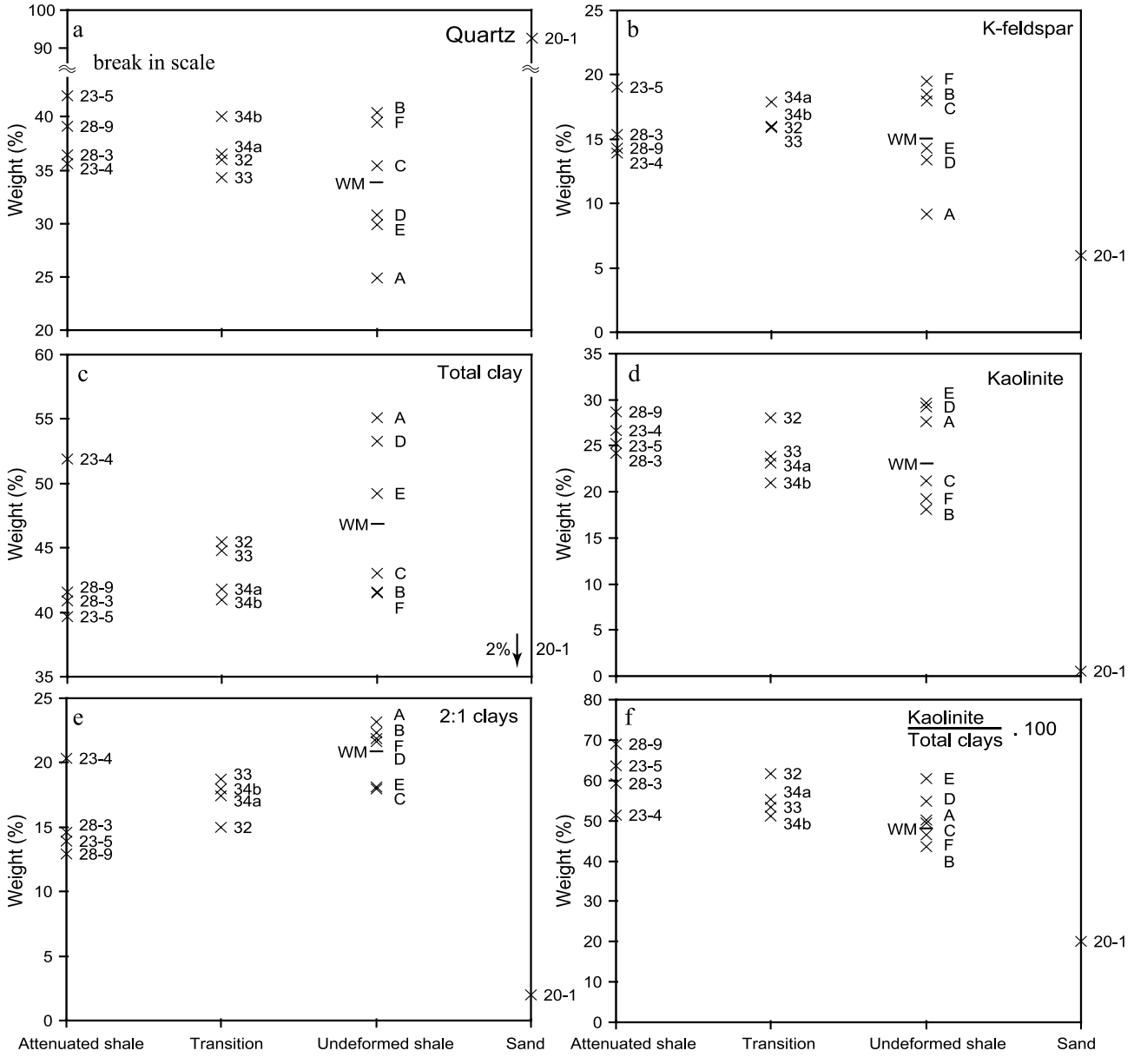

Figure 6. Mineral composition of bulk samples by x-ray diffraction. Analyses marked WM are weighted means across layers A–F (see text for discussion).

(WM in Figure 6a). Layers A, C, D, and E contain both types (I-S-V and K-S-V) of mixed-layer clays. The most quartz-rich layers B and F are significantly different in that the clays are mixtures of pure illite, kaolinite, and smectite. For all layers, the content of mixed-layer clays plus smectite (Figure 7a) and the clay expandability (amount of expandable layers) (Figure 7b) positively correlates with the quartz content (Figure 6a).

The sandstone overlying the Sully vein (sample 20-1) has a total clay content of 2.5% and a quartz content of 92% (Table 1; Figure 6). Clay minerals are kaolinite and illite (Table 2).

Transition and Attenuated Shale

Transition and attenuated shale samples are characterized by a generally higher quartz mineral content relative to undeformed shale samples. The least quartz-rich, and most clay-rich, samples of transition and attenuated shale, samples 32, 33, and 23-4, are, with quartz concentrations of 34–36%, significantly higher in quartz than the most clay-rich layers of the undeformed shale, with quartz contents as low as 25% (Figure 6a). In addition, the mean quartz content of the transition and the attenuated shale samples of 37% is also slightly

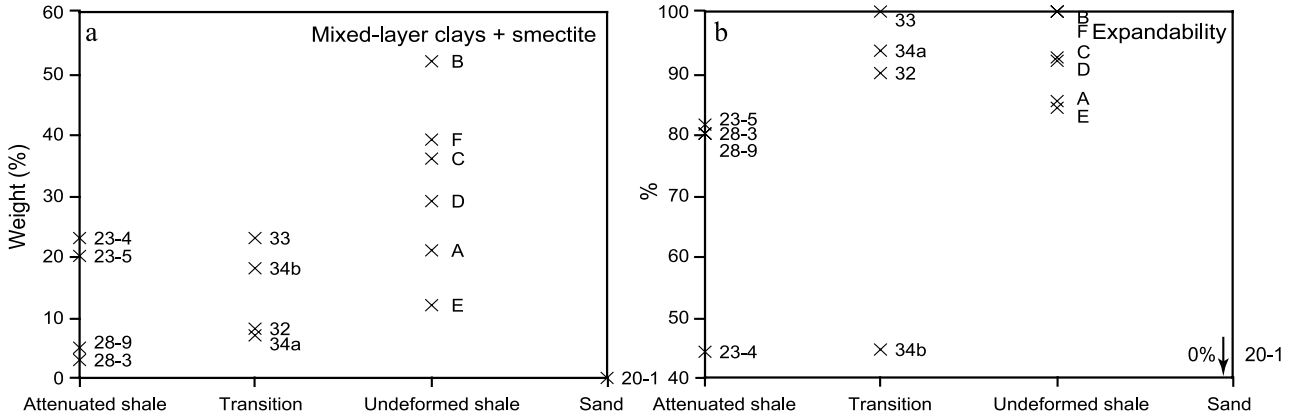

Figure 7. Mineral composition of clay-size fraction by x-ray diffraction.

above the weighted average (34%, Figure 6a) of the six undeformed layers of the Sully vein. Kaolinite values for attenuated shale samples are above those of the more quartz-rich layers B, C, and F (Figure 6d). The mean kaolinite value of transition and attenuated shale samples of 25% is similar to the weighted average of the undeformed shale layers of 23% (Figure 6d).

The mixed-layer clay composition of transition shale samples 34a and b resembles that of undeformed shale A but is distinctly different from the adjacent sandy shale layer B, which does not contain detectable amounts of mixed-layer clays (Table 2). Overall, the abundance of mixed-layer clay in transition and attenuated shale decreases relative to undeformed shale samples, reaching values as low as 3%, compared to the lowest value of 12% in the undeformed shale layer E (Figure 7a). The decrease in mixed-layer clay in the attenuated samples appears accompanied by a corresponding increase in kaolinite as shown by the increasing kaolinite to total-clay ratio (Figure 6f). Expandability in mixed-layer clays is also generally lower in attenuated shale relative to undeformed shale (Figure 7b). Sample 23-4 from the most attenuated part of the fault contains ordered R_1 I-S-V clay in addition to R_0 K-S-V clay.

ELEMENTAL COMPOSITION

Silica, potassium, and aluminum, determined by XRF, follow trends similar to quartz, K-feldspar, and kaolinite, respectively (Figure 8). For instance, the average silica content of all transition and attenuated shale samples of 73% is slightly above the weighted mean of 71% of the undeformed shale layers, which is equal to the silica content of the most quartz-poor attenuated shale sample (sample 23-4) (Figure 8a). Total iron, expressed as Fe_2O_3, decreases from 2.7–9.4% in undeformed shale to $\leq$1% in the most attenuated shale (Figure 8d). Some trace metals, such as cobalt, zinc, and uranium, increase in the transition and attenuated shale samples (Figure 8f–h). Total carbon content is reduced in the attenuated shale samples by 80–90% (Figure 8e).

TEXTURE

Scanning electron microscope images reveal distinct textural changes with faulting (Figure 9). Samples of layers C, E, and F contain only indistinct layering that results from the preferred alignment of some, presumably detrital, clay platelets parallel to bedding (Figure 9a, c, e). Sample 28-9 from the most attenuated part of the fault is characterized by a strong preferred orientation of clay particles approximately parallel to the fault (Figure 9b, d, f). Sample 28-3 from the attenuated shale closer to the source layer exhibited an intermediate stage in fabric development.

PETROPHYSICAL PROPERTIES

Mercury intrusion curves for undeformed shale samples 28-8 (layer C), 28-4 and 28-5 (layer E), and 28-6 (layer F) are characterized by poorly pronounced shoulders and displacement pressures ranging between 31 and 370 psi (0.21 and 2.55 MPa) (Table 3; Figures 5, 10). No significant difference between unjacketed and jacketed experiments is observed for samples of layer E (samples 28-4 and 28-5, respectively), whereas a threefold

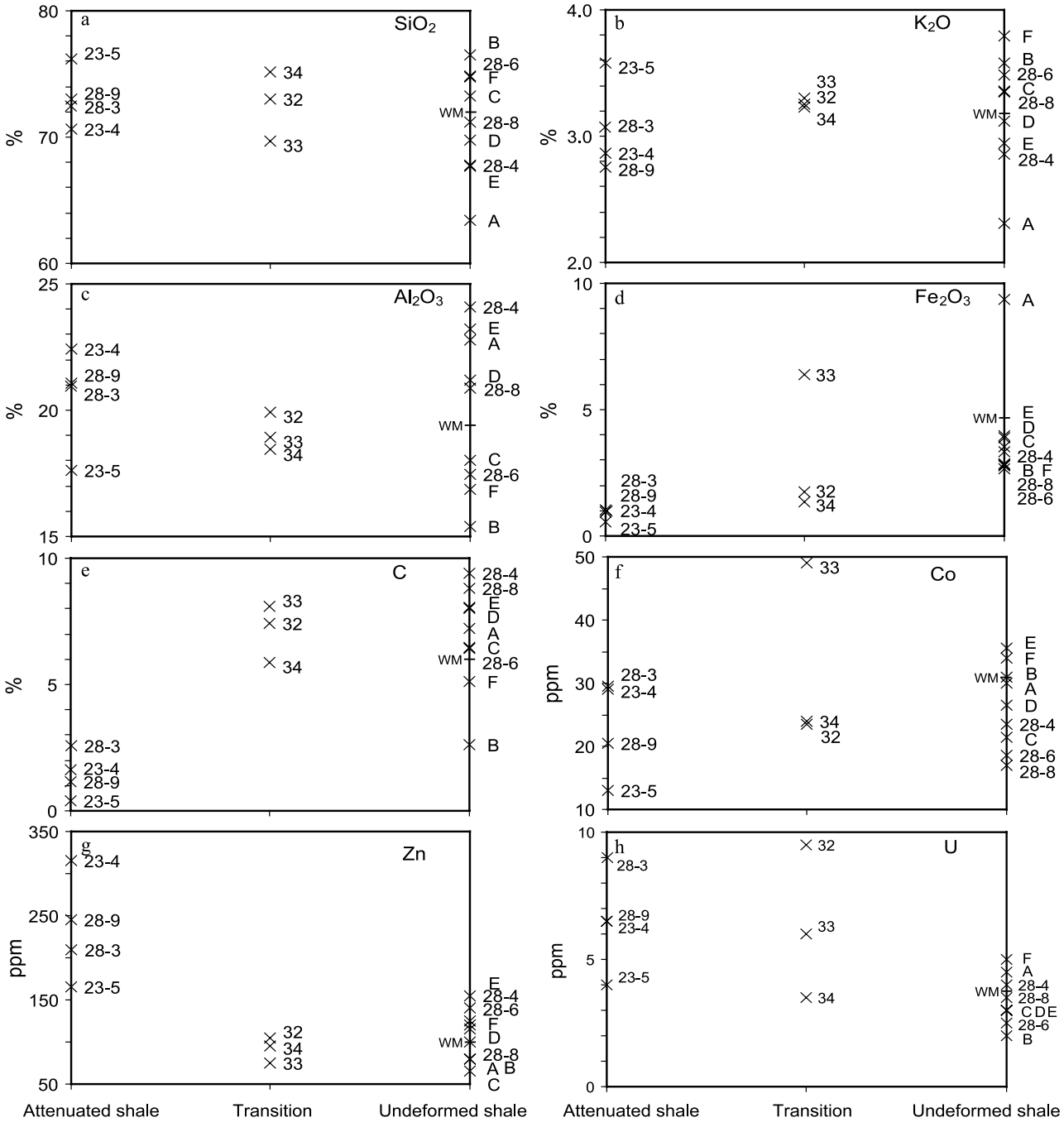

Figure 8. Elemental analyses by XRF for major elements and ICP-MS for trace elements. Oxides are normalized to volatile-free basis. Total iron is as Fe_2O_3. Carbon is by combustion at 1500°C and infrared CO_2 analyzer. Analyses marked WM are weighted means across layers A–F (see text for discussion).

increase in displacement pressure is observed for a jacketed run of sample 28-8 from layer C relative to an unjacketed run of the same sample. Displacement pressures increase, and shoulders are better defined for both jacketed and unjacketed samples of undeformed shale sample 16-1 (layer A) and for the attenuated shale samples. A clay-rich layer of sample 28-9 from the most attenuated part of the deformed shale has a displacement pressure of 1666 psi (11.5 MPa) for the unjacketed sample and 2469 psi (17.0 MPa) for the jacketed sample (Figure 5), reflecting a 50% anisotropy in displacement pressure. These values are 30% higher than undeformed shale A and two orders of magnitude higher than the undeformed sandy shale F.

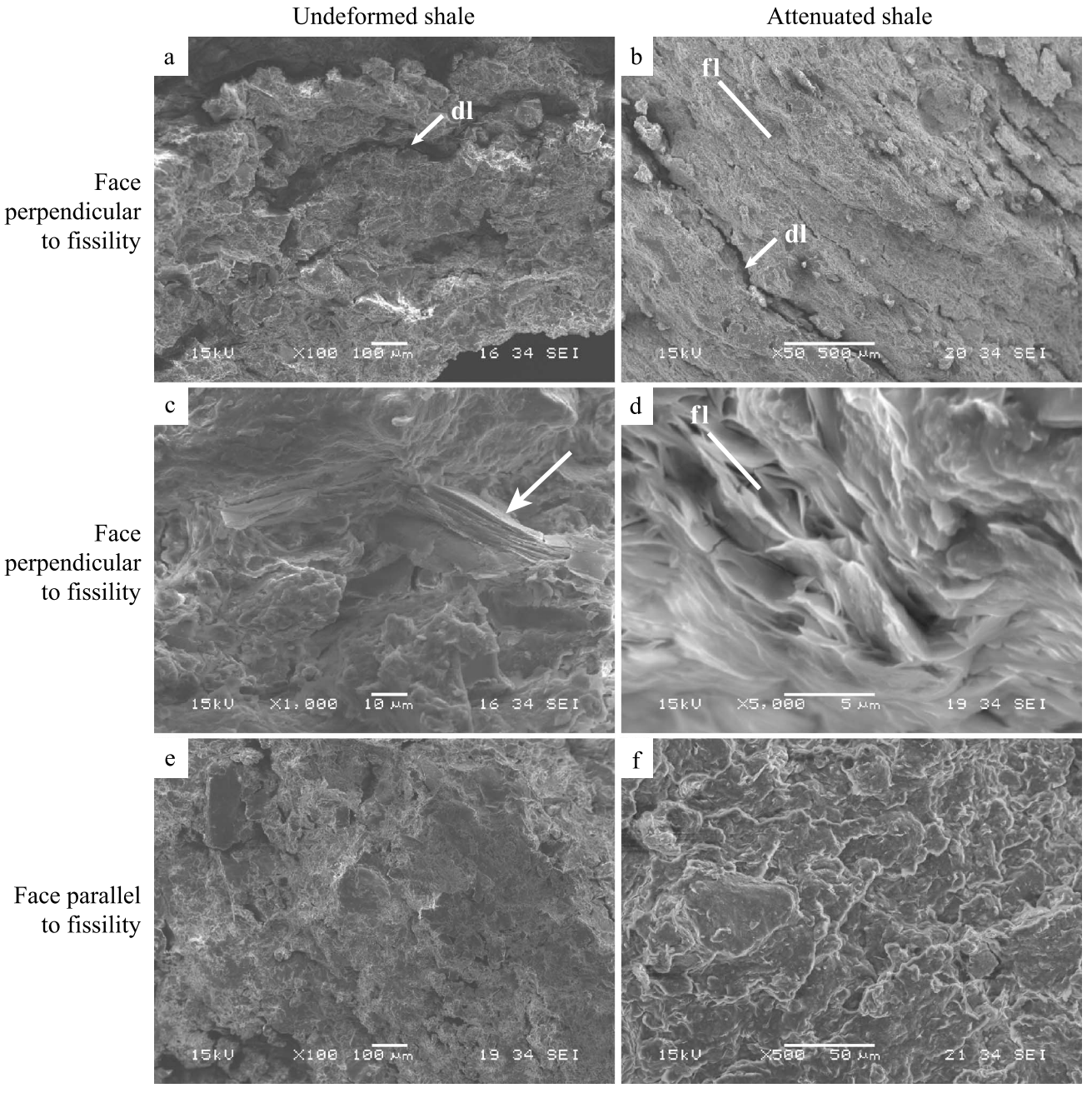

Figure 9. SEM images of the undeformed shale in layer C (sample 28-8) (a, c, e) and deformed shale from the most attenuated part of the Hazel-Atlas fault (sample 28-9) (b, d, f). Layering in undeformed shale is indistinct, recognizable only by the preferred alignment of some clay platelets (arrow in c). Attenuated shale has a strongly developed foliation subparallel to the bounding fault surfaces (fl in b, d). Although care was exercised to minimize sampling artifacts, delamination along foliation planes seen at low magnification in both samples (dl in a, b) may have resulted from dehydration reactions during the sample preparation and may not be representative of subsurface conditions.

Samples of attenuated shale closer to the source layer range between 236 and 608 psi (1.6 and 4.2 MPa) (Figure 5).

Higher displacement pressures reflect a reduction in modal pore-throat aperture and a narrowing in pore-aperture distribution (Figure 11). Modal pore-throat apertures drop from 0.2–0.5 to as low as 0.05 µm for a jacketed analysis of attenuated shale sample 28-9 (Table 3). Pore-throat aperture distributions are generally broad in undeformed samples and narrowly

Table 3. Summary of Mercury Intrusion Analyses

Sample Location	Sample	Entry Pressure (psi)		Displacement Pressure (psi)		Modal Aperture (μm)		Porosity (%)		Permeability K_{air} (md)	
		Unjacketed	Jacketed*	Unjacketed	Jacketed*	Unjacketed	Jacketed*	Unjacketed	Jacketed*	Unjacketed	Jacketed*
Attenuated shale	28-9	1050	1380	1666	2469	0.0706	0.0514	17.5	22.6	0.036	0.022
Attenuated shale	28-1	122		236		0.1095		22.3		0.061	
Attenuated shale	28-2	122		328		0.0907		24.9		0.063	
Attenuated shale	28-3	229	300	470	608	0.0956	0.0955	27.1	30.2	0.091	0.074
Layer F (sandy shale)	28-6	11.8		31		0.4708		23.2		na	
Layer E (shale)	28-4	209		370		0.1904		18.1		0.173	
Layer E (shale)	28-5		160		321		0.1602		19.7		0.124
Layer C (shale)	28-8	22.2	93.4	57	168	0.4215	0.2330	23.5	21.0	3.8	0.371
Layer A (shale)	16-1	736	964	1338	1796	0.0498	0.0437	19.2	18.2	0.023	0.011
Layer A (shale)	repeat	673	806	1299	1712	0.0554	0.0399	18.3	20.7	0.019	0.012

*Samples jacketed to constrain mercury intrusion perpendicular to fissility.

defined in attenuated shale 28-9, with generally better defined maxima in jacketed samples (Figure 11). The better defined pore-throat distribution obtained in the jacketed experiment of sample 28-9 compared to the unjacketed test of the same sample reflects the well-developed textural anisotropy in attenuated shale, whereas these differences are weak for undeformed shale, reflecting its poorly defined textural anisotropy.

Porosity of undeformed shale samples is quite variable, with values ranging between 18 and 24% (Table 3; Figure 5). No significant difference in porosity is observed between undeformed and attenuated shale samples (Table 3; Figure 5), indicating that observed changes in entry and displacement pressure result from a reduction in pore-throat size associated with an increase in textural anisotropy instead of a reduction in porosity.

GRAIN SIZE

Grain size was analyzed for sample 34 from the transition zone and for samples 23-4 and 23-5 of attenuated shale. The mode of all three samples is in the very fine sand-size fraction, leaning toward silt for sample 23-5 and toward fine-grained sand for sample 23-4. Samples 23-5 and 34 have a secondary maximum in the silt-size fraction. These results appear inconsistent with the lighter outcrop color of sample 23-5, suggesting a higher sand content, and its lower clay mineral content, as observed by QXRD analysis compared to sample 23-4. Because these limited grain size results were considered inconclusive, grain size analysis was not extended to the whole sample set.

DISCUSSION

Deformed Shale Composition

The composition of deformed shale samples differs from undeformed samples by a generally higher quartz content and a general increase in kaolinite combined with a corresponding drop in mixed-layer clay abundance and mixed-layer clay expandability. At burial temperatures of less than 60°C, consistent with the subbituminous coal rank (Hunt, 1996), the formation of diagenetic quartz associated with the chemical mass transfer

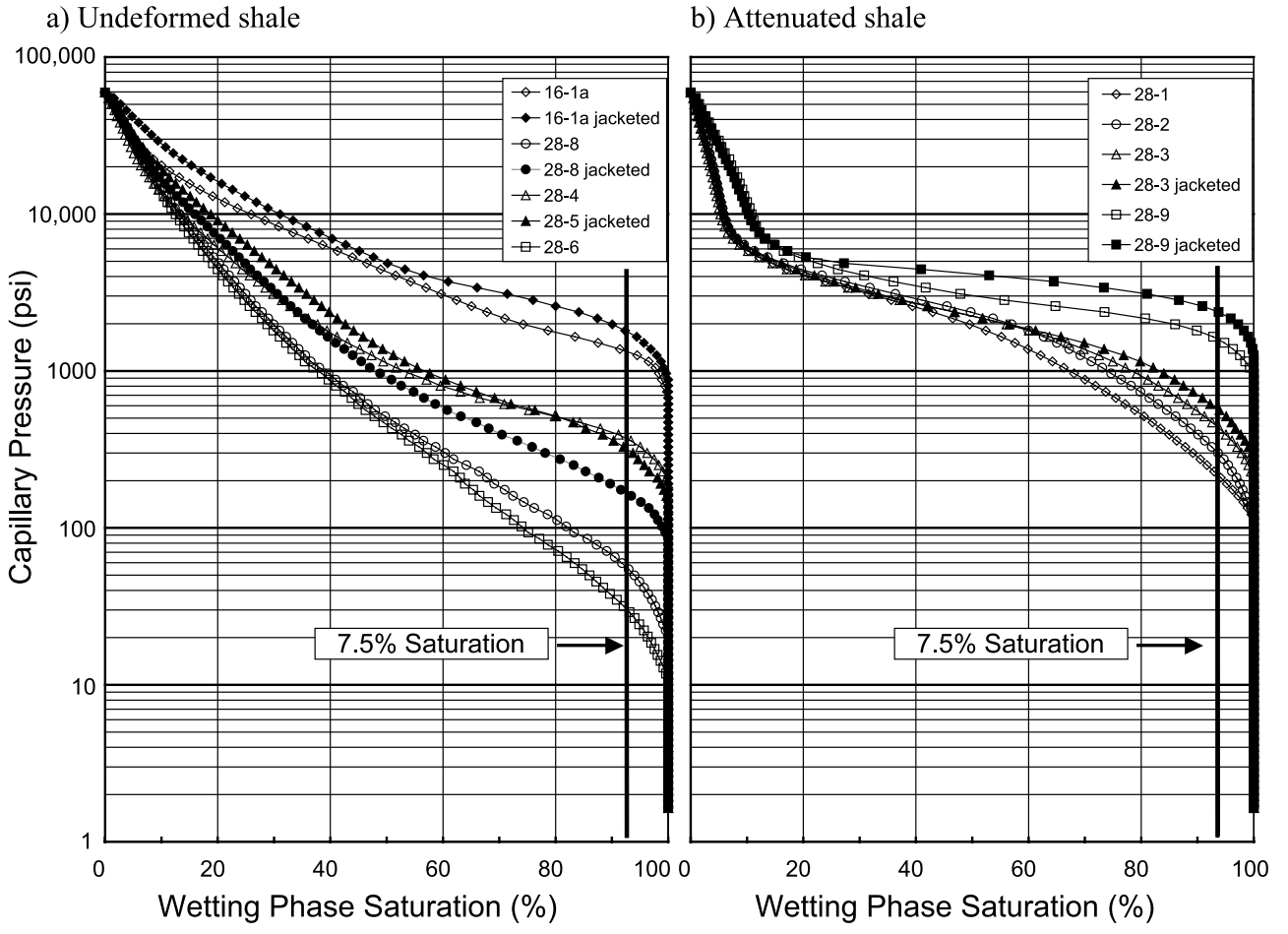

Figure 10. Mercury intrusion curves for undeformed (a) and attenuated (b) shale samples. See Figure 5 for sample locations.

of silica into the fault appears unlikely to be significant. Thus, quartz can be considered a chemically conservative mineral component well suited to assess mechanical mixing of various source layers during shale entrainment and deformation.

The high quartz content of the most clay-rich samples of deformed shale relative to the clay-rich undeformed layers is indicative of mechanical mixing of the clay-rich shale layers with more quartz-rich layers within at least some parts of the deformed shale. The high quartz content of samples 34a and 34b relative to the nearest clay-rich source layer A indicates an effective mechanism of mixing, whereas the rather distinctive mixed-layer clay composition of layer A was largely preserved in transition samples 34a and 34b. Interpreting the sand-rich laminated inclusions and pods in the attenuated shale as remnants of the sand-rich shale layers indicates that the extent of mixing is heterogeneous and varying with position within the fault. Mixing was therefore not extensive enough to result in the homogenization of deformed shale.

The mean quartz content of the attenuated shale samples relative to the weighted average quartz content of the undeformed layers indicates that only about 3% of quartz was added to the attenuated shale from the sandstone that overlies or underlies the Sully vein. This amount is within the resolution limit of the QXRD analysis. A small increase in quartz in attenuated shale is consistent, however, with a 2% increase in mean silica content of attenuated shale relative to the weighted average of the undeformed shale layers. This correspondence between silica and quartz content increases also excludes any significant formation of quartz in the attenuated shale caused by clay diagenesis, confirming the assumption of quartz as a conservative mineral component. Such diagenetic reactions would have resulted in an increase in quartz without a corresponding increase in silica, which is not observed. In contrast, a small contribution of quartz to the attenuated shale from the sandstone is also consistent with our observation of sandstone fragments becoming entrained into the fault at the top of the attenuated shale

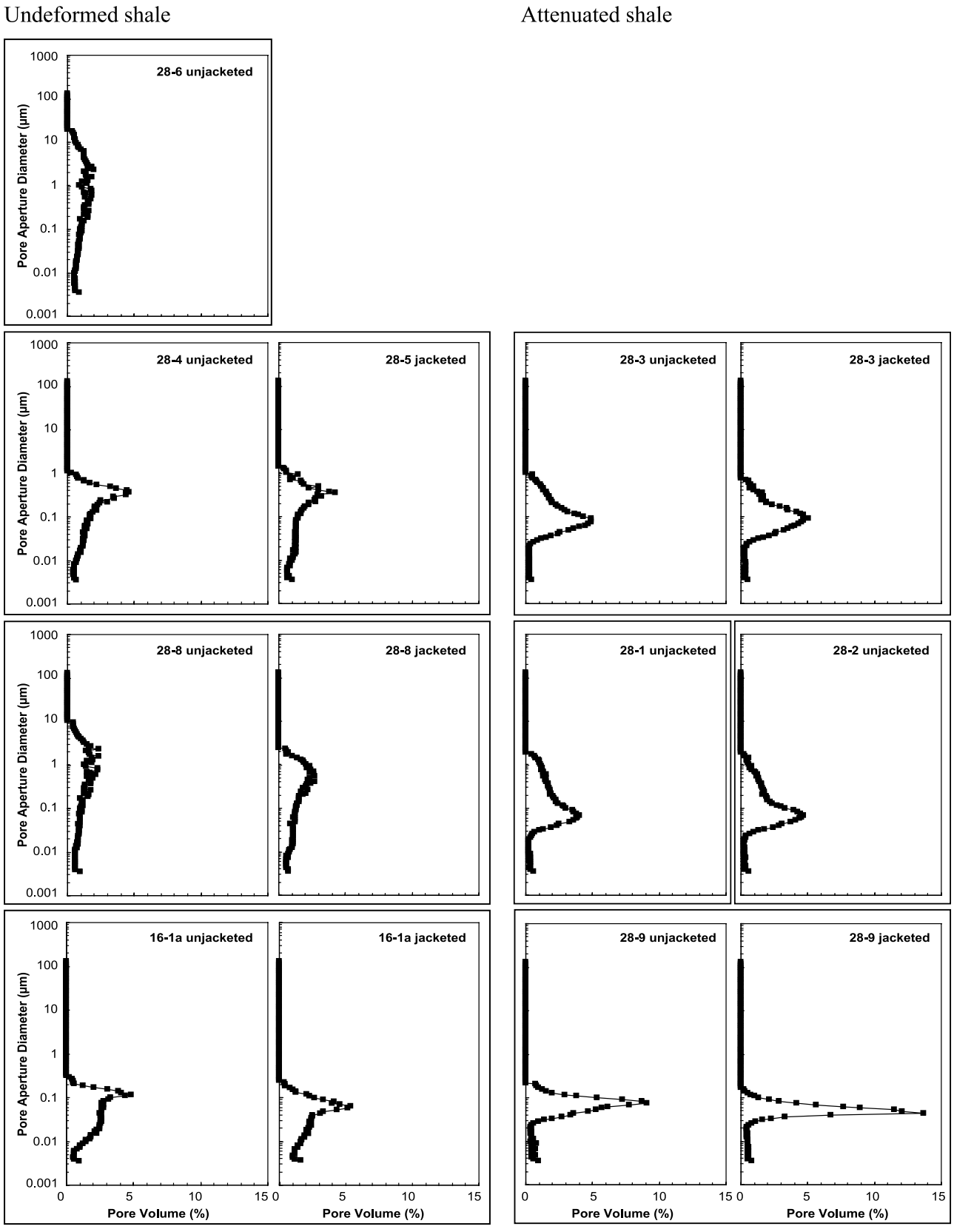

Figure 11. Pore aperture distribution curves for undeformed and attenuated shale samples, based on mercury intrusion experiments.

layer in the hanging wall (Figure 3d). Overall, we notice, however, that this addition of quartz from the over- and underlying sandstone is very small.

Although quartz is, under the given conditions, considered chemically inert, observed trends in clay mineral composition, carbon content, and some trace metals reflect diagenetic changes in shale composition. The roughly inverse correlation between feldspar (Figure 6b) and kaolinite (Figure 6d, f) content of undeformed shale suggests replacement of feldspar by kaolinite. This reaction is favored under acidic conditions (Weaver, 1989), consistent with a positive correlation between kaolinite and carbon content (Figure 8e) of undeformed shales. In addition, the inverse correlation between kaolinite over total clays (Figure 6f) and mixed-layer clay plus smectite content (Figure 7a) among deformed and undeformed shale samples is consistent with the replacement of smectite by kaolinite. A diagenetic replacement of smectite by kaolinite instead of illite is thought to occur under high Al activities (Środoń, 1980) and a low pH (Deer et al., 1992) characteristic of meteoric diagenesis. Acidic conditions and meteoric influx are consistent with the occurrence of the mineral jarosite, which is a common mineral where pyrite dissolution under oxygenated conditions results in the generation of sulfuric acid that causes silicate dissolution (Dana, 1997). The observed enrichment of the deformed shale in certain trace elements may reflect leaching of the surrounding sandstone by meteoric fluids and precipitation along the fault. Interaction with oxidizing fluids may also explain the reduction in organic matter content within the deformed shale. A causal connection between illite-smectite to kaolinite transformation and acidic water flow is supported by the similarity of trends in kaolinite to total-clay ratios (Figure 6f) and in metal concentrations (Figure 7g–h) across the sampling transect.

The higher ratio of kaolinite to total clays and lower carbon content of attenuated shale compared to undeformed shale seems to suggest that acidic and oxygenated meteoric water infiltrated the attenuated shale more effectively than the undeformed shale. Preferred fluid infiltration into the attenuated shale is unexpected, however, in view of its lower permeability relative to the undeformed shale (Table 3). Enhanced fluid access could have been contemporaneous with the mechanical sliding and rotation of clay minerals during faulting. Although the sampling geometry was not designed to specifically address compositional heterogeneity across the deformed shale, it appears that the compositional trends within the deformed shale scale with the intensity of deformation, as assessed macroscopically and by SEM, instead of distance from the porous sandstone. Gradients in alteration within the deformed shale as a function of distance from adjacent sandstone would be expected for shale alteration that postdates faulting. The apparent absence of such gradients is consistent with synfaulting fluid access to the deformed shale, resulting in enhanced diagenetic alteration.

Deformation Mechanisms

Models of shale entrainment into faults by previous workers can be grouped into four fundamental deformation mechanisms (Figure 12).

1. Mechanical wear, i.e., erosion, of the fault surfaces (Figure 12a) results in the removal or plucking of grains from the wall rock and their incorporation into the fault rock during fault slip. This process may cause grain size reduction either as part of the wear process or because of shear within the fault rock. In a simple case, the amount of wear is uniform for shale and sand layers. The fault rock composition would thus correspond to the composition of the host rock integrated over the slip distance. It is our interpretation that this model underlies currently applied methods of predicting the sealing capacity of faults such as the shale gouge ratio of Yielding et al. (1997; Yielding, 2002). Grain size reduction would potentially increase the silt- or clay-size fraction in the shale. The amount of clay minerals, however, would be unaffected except for chemical diagenetic reactions that, aided by grain size reduction, transform nonclay minerals such as feldspar into clay minerals. A variant of the wear model (Sperrevik et al., 2002) assumes that less resistant layers are abraded at a higher rate, resulting in a wider fault core in the soft layers and in more material of the softer layer included in the fault rock.
2. Entrainment of shale between two overlapping fault segments (Figure 12b) was proposed by Weber et al. (1978) and discussed further by Lehner and Pilaar (1997), Koledoye et al. (2000, 2003), Aydin and Eyal (2002), Doughty (2003), and Davatzes and Aydin (2005). The two overlapping fault segments form an extensional or, apparently less common, contractional step, with slip transfer across the intervening shale. With increasing slip, the shale between these overlapping fault segments is drawn

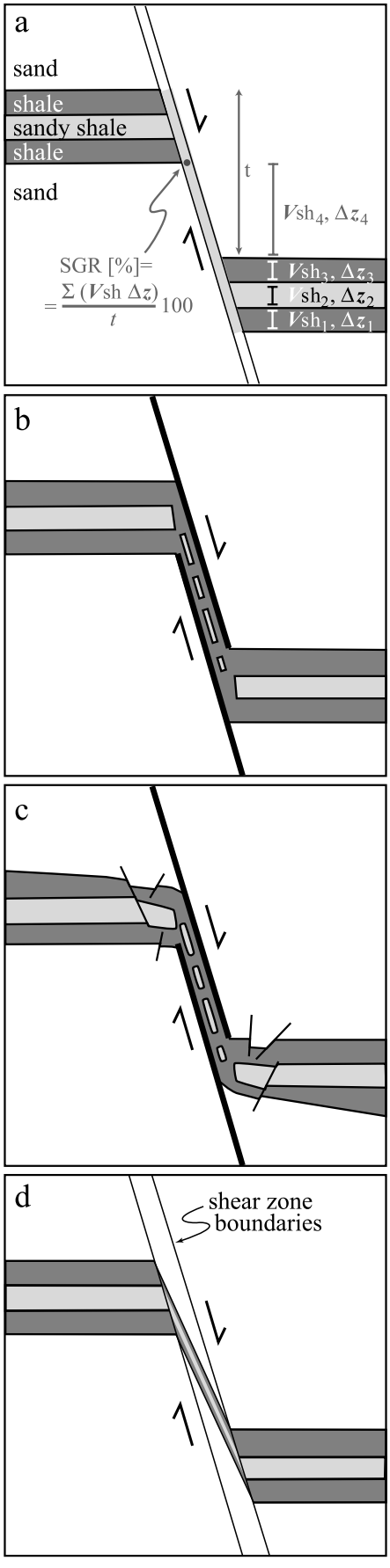

out ductilely, whereas the over- and underlying sandstone deforms brittlely. In sequences with multiple sand and shale horizons, the stacking of fault steps results in a layered fault zone containing boudinaged sand layers and thinned shale layers as described in a field example by Aydin and Eyal (2002). The internal deformation of the shale layer reflects thinning of the shale layer perpendicular to and extension parallel to the fault surfaces, in combination with shear parallel to the fault surfaces. Fault-parallel shear is partitioned among the bounding fault surfaces, possible internal slip surfaces, and distributed shear of the shale. The thickness and length of the deformed shale would be controlled by the step width between the overlapping fault segments. This step width appears to be some function of the thickness of the shale layer based on the observation that a larger step width is typically associated with thicker shale layers and narrower step widths are associated with thinner shale beds. Because of the thinning of the deformed shale layer in the fault, the deformed shale is a condensed section of the shale outside the fault. Therefore, the composition of the shale in the fault is expected to correspond to the shale composition outside the fault. For the simple geometry shown in Figure 12b, the amount of shale does not balance volumetrically relative to the over- and underlying sandstone layers, requiring an addition of shale for an extensional fault-step geometry.

3. Extrusion of shale from the source bed into the fault (Figure 12c) was invoked by Lehner and Pilaar (1997) and described by van der Zee et al. (2003) to account for the volume balance of shale within faults that are composed of extensional fault steps. The extrusion of shale from the source layer into the fault would result in local thinning of the source bed, accommodated in the over- and underlying sandstone layers by slip along subsidiary faults. Lehner

Figure 12. Mechanisms of shale entrainment along faults by (a) mechanical wear and mixing, (b) linkage across fault step, (c) shale intrusion from source layer, and (d) simple shear. Based in part on Weber et al. (1978), Lindsay et al. (1993), Yielding et al. (1997), and Aydin and Eyal (2002). Gray scale correlates with clay mineral content, with darker shades indicating higher clay content. Calculation of shale gouge ratio (SGR) for a point along the fault is given in (a) after Yielding (2002), with SGR as a function of throw t, clay mineral content Vsh, and layer thickness Δz, and indices 1–4 designating layers 1–4. Vsh = Vshale.

and Pilaar (1997) envisioned that such extrusion would occur by granular flow of the shale.

4. Entrainment of shale by simple shear between two parallel bounding surfaces was proposed by Lindsay et al. (1993), a process they referred to as shear smear. In contrast to the overlapping fault model, no slip would occur along the bounding surfaces. Instead, slip is distributed across the fault zone similar to a ductile shear zone and accommodated by simple shear.

These deformation mechanisms are not mutually exclusive. For instance, the entrainment of shale by fault overlap could be combined with shale extrusion. Furthermore, wear could accompany slip along overlapping faults.

The shale gouge ratio of Yielding et al. (1997) (Figure 12a), consistent with the wear model, predicts a clay mineral component in the attenuated shale of the Hazel-Atlas fault of 13%, which is significantly below the measured clay mineral content of 47%. Although the incorporation of a small component of host sandstone into the attenuated shale is considered likely, this discrepancy between shale gouge ratio and actual clay mineral content is inconsistent with a mechanical wear model. Instead, the attenuated shale composition is similar to that of the undeformed shale, indicating that the attenuated shale was predominantly derived from the undeformed shale layer with little contribution from the sandstone layers above and below. This is consistent with any of the remaining three mechanisms discussed above. The orientation of subsidiary faults, oriented in part at high angle to the overall fault orientation, is inconsistent with the shear smear model of Lindsay et al. (1993). The Sully vein in the hanging wall also does not thin noticeably in the vicinity of the fault that would indicate extrusion of shale from the source layer into the fault.

The composition of the most clay-rich layers in the deformed shale requires mixing of the shale on a less than 2-cm (0.78-in.) scale, the size of the core plugs, and over a short slip distance. The internal composition of the deformed shale in the Hazel-Atlas fault is thus not in agreement with models that assume the preservation of the stratigraphy of the undeformed shale, albeit condensed and stretched parallel to the fault. Instead, the mineralogical composition of the deformed shale indicates mixing of clay-rich and sand-rich layers of the Sully vein. In addition, the locally preserved primary depositional contact between the footwall sandstone and the deformed shale observed in the haulage level is inconsistent with the overlapping fault model as portrayed in Figure 12b.

To account for these observations, we envision the fault evolution as follows (Figure 13), recognizing that incipient stages of fault evolution are not directly observed but inferred based on mutual crosscutting relations of sequentially forming structures. Based on the occurrence of a zone of deformation bands in the footwall of the fault and following field observations of similar faults with incipient shale entrainment by Davatzes and Aydin (2005), we infer that the incipient stage of shale entrainment occurred by distributed deformation across a zone of subparallel deformation bands in the sandstone that over- and underlies the shale layer (stage 1 in Figure 13). These deformation bands have a normal sense of slip and are oriented parallel to the evolving fault zone. The zone of deformation bands is preserved in the machinery level as the cemented layer in the footwall contact of the deformed shale. The distributed shear results in the bending and synthetic rotation of the shale layer relative to the overall sense of faulting. With increasing deformation, steeply dipping faults form with synthetic sense of slip relative to the overall fault slip (stage 2 in Figure 13). These faults crosscut earlier deformation bands and offset bedding within the laminated deformed shale, resulting in the stair-stepping geometry of deformed shale as observed in the haulage level. Sedimentary layering within the deforming shale is still preserved but tilted in the direction of faulting. Continued fault slip results in increasing granular flow of the clay-rich part of deforming shale, stretching and boudinaging the more sand-rich layers and mixing of clay- and sand-rich parts. Increasing slip leads to the localization of deformation along slip surfaces either within the shale core or along the shale-sandstone interfaces of the fault zone (stage 3 in Figure 13).

Distributed deformation during incipient stages of fault evolution is interpreted to be the result of differences in deformation behavior, with sandstone deforming by localized modes of failure whereas shale deforms by distributed granular flow. Although failure of the sandstone is depicted in Figure 13 by multiple parallel deformation bands, failure may, in other instances, involve the formation of joints and shearing of joints. Similar to the shear smear model, distributed shear during early fault development affects the shale layer and the immediately over- and underlying sandstone equally, thus maintaining a volume balance. With increasing fault slip, discrete slip surfaces develop similar to the overlapping fault model, without requiring

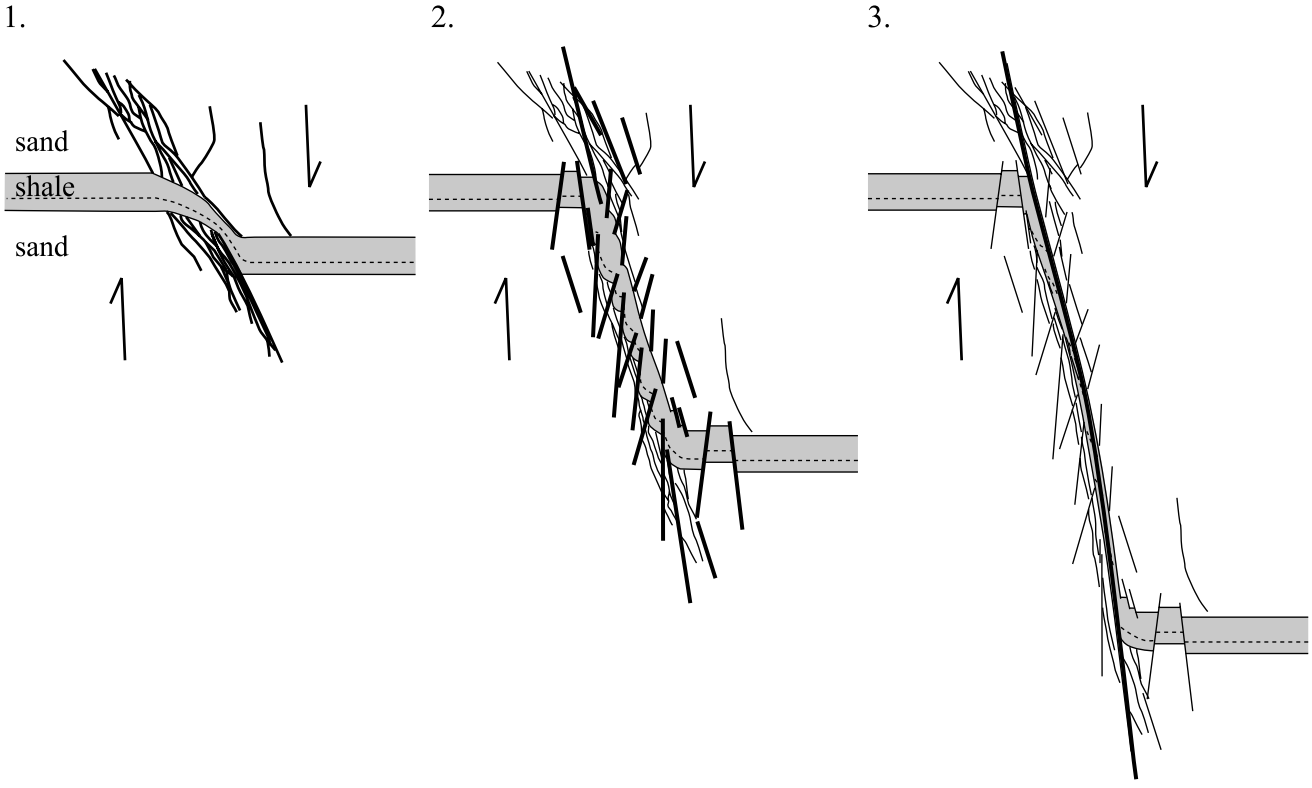

Figure 13. Schematic representation of shale entrainment along an evolving normal fault. (1) The fault initiates through a zone of subparallel deformation bands in the sandstone that over- and underlies the shale layer. Normal slip along these deformation bands results in the bending and rotation of the shale layer in a synthetic sense relative to the overall fault slip direction. (2) With increasing deformation, steeply dipping faults form that truncate earlier formed deformation bands and bedding (dotted lines). Offset along these steeply dipping faults results in the stair stepping of bedding within the deforming shale. (3) Slip localizes within the shale due to granular flow, leading to the formation of discrete slip surfaces in the deforming shale or along the shale-sandstone interfaces. Sandy layers become boudinaged and elongated in the shale. The Hazel-Atlas fault is envisioned to correspond to stage 2 in the haulage level and to a beginning stage 3 in the machinery level. Stage 1 is inferred based on the presence of deformation bands in the footwall and modified after field observations by Davatzes and Aydin (2005). Active structures during each stage are highlighted in bold.

flow of shale into the fault. Because the interface between shale and sandstone is not a slip surface during the early stages of fault development, no entrainment of sand is expected from the sandstone of the foot- and hanging wall into the deforming shale. Further slip and shear localization and the development of slip surfaces along the interfaces between deforming shale and the adjacent sandstone may result in the incorporation of sand into the deforming shale by mechanical wear.

Implications for the Sealing Capacity of Faults

The difference in clay mineral content of the deformed shale compared to that predicted by the shale gouge ratio of Yielding et al. (1997) is likely to be significant for seal prediction. Following Yielding et al. (1997) and Fristad et al. (1997), a shale gouge ratio of 13% would be insufficient for a sealing fault, whereas the actually measured clay mineral content of 47% would, according to their reservoir fluid pressure data, represent a good seal, capable of sustaining an across-fault pressure difference of 0.4–0.6 MPa. Similar calibration values were obtained by Gibson (1994; column height values are converted to across-fault pressure difference by Yielding et al., 1997) and somewhat lower values (0.25 MPa) by Sverdrup et al. (2003). Doughty (2003) suggested that the shale gouge ratio could serve as a predictor of sealing potential of faults with slip large enough to segment the attenuated shale and detach segments from the source bed. Fault slip along the Hazel-Atlas fault has been insufficient to detach the

attenuated shale from the source bed in the hanging-wall exposure.

The increase in the displacement pressure from undeformed to attenuated shale by up to two orders of magnitude without a concurrent increase in clay mineral content also demonstrates that the sealing capacity is not a linear function of clay mineral content of the deformed shale as commonly assumed. Similar increases in mercury entry pressures by up to one order of magnitude were also reported by Hippler (1997) for macroscopically matching samples of undeformed and naturally deformed clay-rich sandstones or siltstones. These observations do not exclude clay mineral content as a significant parameter in controlling sealing capacity as demonstrated by laboratory measurements of artificial clay mixtures (Crawford et al., 2002) and of outcrop and core samples (Manzocchi et al., 1999). It does indicate, however, that other parameters can be equally or more significant. The lack of a consistent trend in porosity from undeformed to deformed shale also demonstrates that the porosity of the shale alone is not a dominant factor in controlling sealing capacity. This is consistent with earlier findings of Neuzil (1994) and Dewhurst et al. (1999), who noted a general weak correlation between mudrock porosity and permeability.

Our SEM observations of a distinct change in shale fabric suggest that the preferred alignment of platy minerals is a significant parameter in shale-sealing capacity. The effect of the preferred clay mineral alignment on flow-path tortuosity and, thus, on permeability associated with shearing was demonstrated experimentally by Arch and Maltman (1990) and Dewhurst et al. (1996). The effect of mineral alignment on pore aperture distribution and, thus, on capillary pressure is less clear. Preferred alignment will be controlled by the clay mineral volume percentage, clay mineral composition, as well as the clay mineral size distribution relative to the abundance of nonclay minerals. The size distribution of clay minerals will be a function of clay mineralogy, depositional conditions, and clay diagenesis, with detrital micas and kaolinite commonly being larger than diagenetic smectite. As noted by Djéran-Maigre et al. (1998), kaolinite tends to form stacks that result in less well-developed fabrics compared to illite and smectite clays. Dewhurst et al. (1996) reported a higher anisotropy in permeability for smectite-rich clay than for kaolin clay. Thus, the depositional environment, pore-water composition, and burial history could affect the sealing capacity significantly. Generally higher capillary displacement pressures in kaolinite clays were noted by Bretan et al. (2003) and observed by P. D'Onfro (2002, unpublished industry data) elsewhere.

Sperrevik et al. (2000) suggested that the entrainment of shale into faults is affected by the degree of ''lithification'' or compaction prior to faulting. Following Hinch (1980) and Katsube and Williamson (1998), the compaction behavior of mudrocks changes from a regime dominated by mechanical compaction to one of predominant chemical compaction with prograded burial. The deformation behavior of shale in faults may change in a similar way with increasing burial depth. In addition, compaction and smearing behavior of shale is likely to depend on the mineralogical composition of the shale, including the ratio of clay minerals to quartzofeldspathic grains, and the clay mineral composition of detrital clay, particularly the smectite component in illite-smectite mixed-layer clay.

Diagenetic clay neoformation and precipitation of carbonate cement will also tend to occlude pores and thus increase sealing capacity. Clay neoformation in deformed shale within faults was observed by Pevear et al. (1997) and Vrolijk and van der Pluijm (1999). The effects of diagenetic reactions other than clay mineral diagenesis on shale permeability and pore structure were documented by Katsube and Williamson (1994, 1998) for undeformed shales. The extent of these reactions will depend on initial shale composition, including organic matter content, pore-fluid composition, and burial temperature. A positive correlation of carbonate content and sealing capacity of shale that could reflect diagenetic occlusion of pore apertures is seen in the data set of Krushin (1997). In addition, clay mineralogy and pore-water chemistry control physicochemical surface properties of clay minerals that affect pore structure (Mesri and Olson, 1971) and, thus, membrane-sealing behavior. The significance of the pore-fluid composition for the fault-sealing capacity was emphasized by Bretan et al. (2003).

Our results indicate that the sealing capacity of deformed shale in faults is, at least in our example, significantly underestimated based on simple mixing laws of clay and nonclay minerals. In conjunction with previous studies on shale petrophysical properties, we conclude that predictive algorithms of shale-sealing capacity require a multiparameter approach to be applicable outside a restricted range of depositional and structural settings. We propose that such predictive algorithms have to account for the initial shale composition and stratigraphy, changes in shale entrainment

mechanism with increasing fault slip, clay fabric development, and changes in shale composition caused by burial diagenetic reactions.

CONCLUSIONS

The entrainment of shale from the Sully vein into the Hazel-Atlas normal fault resulted in the attenuation of the 1.6-m (5-ft)-thick source layer to 5 cm (2 in.). Detailed quantitative mineralogical and elemental analyses indicate that the mean quartz content of the attenuated shale is equal to or slightly above the mean quartz content of the undeformed shale, indicating that little quartz is incorporated from the over- and underlying sandstone into the attenuated shale by mechanical wear along the fault surfaces. This finding is in contrast to models of shale entrainment by mechanical wear and mixing that underlie predictive models such as the shale gouge ratio of Yielding et al. (1997). Instead, shale entrainment is interpreted to result from incipient distributed shear along a zone of deformation bands, granular flow of the shale, and the increasing localization of deformation in the shale core of the fault zone, leading to the formation of discrete slip surfaces in the shale core or along the shale-sandstone interfaces. Because fault-parallel slip surfaces are not formed during early and intermediate stages of fault development, mechanical wear along the sand-shale interfaces is insignificant during these stages of faulting. The quartz and silica content of deformed shale that is highest in clay content was found to be significantly higher than that of the three most clay-rich undeformed layers, indicative of mixing of clay- and sand-rich shale layers by granular flow in the deforming shale.

Capillary displacement pressures of deformed shale increase by 30% relative to the undeformed shale of highest sealing capacity and by up to two orders of magnitude compared to sand-rich layers of undeformed shale. Based on SEM observations and a 50% anisotropy in capillary displacement pressure of deformed shale, we conclude that this increase in sealing capacity results from the formation of a preferred grain alignment in the attenuated shale approximately parallel to the fault zone. A decrease in mixed-layer clay content and a corresponding increase in kaolinite content with deformation likely reflects synfaulting clay diagenesis and may have contributed to an increase in sealing capacity.

Our results emphasize the significance of textural changes with deformation and of synfaulting diagenesis in controlling the sealing capacity of faults containing shale. These processes are likely governed by multiple parameters, including clay mineral volume fraction, clay mineral composition, grain size and grain shape distribution, physical and chemical shale diagenesis prior to faulting, pore-fluid composition, and the reactiveness of the fault rock mineral phases to undergo syn- and postfaulting chemical alteration. We propose that improved predictions of fault seal by shale entrainment require a multiparameter approach that integrates structural, stratigraphic, petrophysical, and geochemical observations.

APPENDIX: X-RAY DIFFRACTION ANALYSIS OF CLAY-SIZE FRACTION

Samples selected for detailed study of the clay-size fraction (<2 μm equivalent spherical diameter) were treated to remove carbonate and Fe-iron oxide cements with Na-acetate buffer and Na-dithionate, respectively (Jackson, 1985). The Na^+-saturated clays were exchanged with Ca^{2+} using calcium cation exchange resin beads. Approximately 250 mL of less than 2-μm suspension was shaken overnight with about 5 g of Dowex HCR-W2 resin beads. The suspension was then dried, and oriented aggregates were made by evaporation onto glass slides to provide a sample approximately 4 cm (1.5 in.) long with a minimum amount of clay of 10 mg/cm^2 (Moore and Reynolds, 1997). Diffraction scans of air-dried and ethylene glycol-solvated samples were collected with a Scintag X1 diffractometer equipped with a solid-state Si detector. The scans were made from 2 to 52° 2θ with a 0.02° 2θ step increment and counting rate of 4 s/step or longer using Cu K_α radiation transmitted through a 2.0-mm (0.078-in.) divergence and 4-mm (0.157-in.) scatter slit. Detector slits were 0.5 and 0.2 mm (0.019 and 0.0078 in.).

We applied a full-pattern computer simulation following Drits et al. (1997, 2002) and Sakharov et al. (1999) to reveal the structural details of complex clay mineral mixtures such as three-component mixed-layer types having 2:1 layers with variable charge density and different d001 values. The multispecimen-fitting technique of Sakharov et al. (1999) was used to simulate diffraction data from both the ethylene glycol-treated and air-dried scans of the same sample. The result was judged to be reasonable when the best fit was obtained for both of these simulations using the same structural parameters.

REFERENCES CITED

Arch, J., and A. Maltman, 1990, Anisotropy permeability and tortuosity in deformed wet sediments: Journal of Geophysical Research, v. 95, p. 9035–9045.

Aydin, A., and Y. Eyal, 2002, Anatomy of a normal fault with shale smear: Implications for fault seal: AAPG Bulletin, v. 86, p. 1367–1381.

Bailey, S. W., 1980, Summary of recommendations of AIPEA Nomenclature Committee on clay minerals: American Mineralogist, v. 65, p. 1–7.

Berg, R. R., 1975, Capillary pressures in stratigraphic traps: AAPG Bulletin, v. 59, p. 939–956.

Bouvier, J. D., C. H. Kaars-Sijpesteijn, D. F. Kluesner, C. C. Onyejekwe, and R. C. Van Der Pal, 1989, Three-dimensional seismic interpretation and fault sealing investigations, Nun River field, Nigeria: AAPG Bulletin, v. 73, p. 1397–1414.

Bretan, P., G. Yielding, and H. Jones, 2003, Using calibrated shale gouge ratio to estimate hydrocarbon column heights: AAPG Bulletin, v. 87, p. 397–413.

Brown, A., 2003, Capillary effects on fault-fill sealing: AAPG Bulletin, v. 87, p. 381–395.

Childs, C., J. J. Walsh, and J. Watterson, 1997, Complexity in fault zone structure and implications for fault seal prediction, *in* P. Møller-Pedersen and A. G. Koestler, eds., Hydrocarbon seals. Importance for exploration and production: Amsterdam, Elsevier, p. 61–72.

Chung, F. H., 1974, Quantitative interpretation of x-ray diffraction patterns of mixtures: I. Matrix-flushing method for quantitative multicomponent analysis: Journal of Applied Crystallography, v. 7, p. 519–525.

Cooper, H. M., N. H. Snyder, R. F. Abernethy, E. C. Tarpley, and R. J. Swingle, 1947, Analyses of miner, tipple, and delivered samples, *in* Analyses of Arizona, California, Idaho, Nevada, and Oregon coals: U.S. Department of the Interior Bureau of Mines Technical Paper, v. 696, p. 27–47.

Crawford, B. R., R. D. Myers, A. Woronow, D. R. Faulkner, and E. H. Rutter, 2002, Porosity-permeability relationships in clay-bearing fault gouge: Society of Petroleum Engineers/International Society of Rock Mechanics, Rock Mechanics Conference Paper 78214, Irving, Texas, 13 p.

Dana, J. D., 1997, Dana's new mineralogy: The system of mineralogy of James Dwight Dana and Edward Salisbury Dana: New York, Wiley, 1819 p.

Davatzes, N. C., and A. Aydin, 2005, Distribution and nature of fault architecture in a layered sandstone and shale sequence: An example from the Moab fault, Utah, *in* R. Sorkhabi and Y. Tsuji, eds., Faults, fluid flow, and petroleum traps: AAPG Memoir 85, 153–180.

Davis, F. F., and H. B. Goldman, 1958, Mines and mineral resources of Contra Costa County, California: California Journal of Mines and Geology, v. 54, p. 501–583.

Deer, W. A., R. A. Howie, and J. Zussman, 1992, An introduction to the rock-forming minerals, 2d ed.: Harlow, United Kingdom, Longman, 696 p.

Dewhurst, D. N., M. B. Clennell, K. M. Brown, and G. K. Westbrook, 1996, Fabric and hydraulic conductivity of sheared clays: Géotechnique, v. 46, p. 761–768.

Dewhurst, D. N., Y. Yang, and A. C. Aplin, 1999, Permeability and fluid flow in natural mudrocks, *in* A. C. Aplin, A. J. Fleet, and J. H. S. Macquaker, eds., Muds and mudrocks: Physical and fluid flow properties: Geological Society (London) Special Publication 158, p. 23–43.

Djéran-Maigre, I., D. Tessier, D. Grunberger, B. Velde, and G. Vasseur, 1998, Evolution of microstructures and of macroscopic properties of some clays during experimental compaction: Marine and Petroleum Geology, v. 15, p. 109–128.

Doughty, P. T., 2003, Clay smear seals and fault sealing potential of an exhumed growth fault, Rio Grande rift, New Mexico: AAPG Bulletin, v. 87, p. 427–444.

Drits, V. A., and C. Tchoubar, 1990, X-ray diffraction by disordered lamellar structures: Theory and applications to microdivided silicates and carbons: Berlin, Springer, 371 p.

Drits, V. A., H. Lindgreen, and A. Salyn, 1997, Determination by x-ray diffraction of content and distribution of fixed ammonium in illite-smectite. Application to North Sea illite-smectites: American Mineralogist, v. 82, p. 79–87.

Drits, V. A., H. Lindgreen, B. A. Sakharov, H. J. Jakobsen, A. Salyn, and L. G. Dainyak, 2002, Tobelitization of smectite during oil generation in oil-source shales. Application to North Sea illite-tobelite-smectite-vermiculite: Clays and Clay Minerals, v. 50, p. 82–98.

Fristad, T., A. Groth, G. Yielding, and B. Freeman, 1997, Quantitative fault seal prediction: A case study from Oseberg Syd, *in* P. Møller-Pedersen and A. G. Koestler, eds., Hydrocarbon seals. Importance for exploration and production: Amsterdam, Elsevier, p. 107–124.

Gibson, R. G., 1994, Fault-zone seals in siliciclastic strata of the Columbus basin, offshore Trinidad: AAPG Bulletin, v. 78, 1372–1385.

Gibson, R. G., 1998, Physical character and fluid-flow properties of sandstone-derived fault zones, *in* M. P. Coward, T. S. Daltaban, and H. Johnson, eds., Structural geology in reservoir characterization: Geological Society (London) Special Publication 127, p. 83–97.

Goodyear, W. A., 1877, The coal mines of the western coast of the United States: San Francisco, Bancroft, 153 p.

Harris, D., G. Yielding, P. Levine, G. Maxwell, P. T. Rose, and P. Nell, 2002, Using shale gouge ratio (SGR) to model faults as transmissibility barriers in reservoirs: An example from the Strathspey field, North Sea: Petroleum Geoscience, v. 8, p. 167–176.

Heum, O. R., 1996, A fluid dynamic classification of hydrocarbon entrapment: Petroleum Geoscience, v. 2, p. 145–158.

Hinch, H. H., 1980, The nature of shales and the dynamics of hydrocarbon expulsion in the Gulf Coast Tertiary section, *in* W. H. Roberts III and R. J. Cordell, eds., Problems of petroleum migration: AAPG Studies in Geology 10, p. 1–18.

Hippler, S. J., 1997, Microstructures and diagenesis in North Sea fault zones: Implications for fault-seal potential and fault-migration rates, *in* R. C. Surdam, ed., Seals, traps, and the petroleum system: AAPG Memoir 67, p. 85–101.

Hunt, J. M., 1996, Petroleum geochemistry and geology, 2d ed.: New York, Freeman, 743 p.

Ingram, R. L., 1953, Fissility of mudrocks: Geological Society of America Bulletin, v. 64, p. 869–878.

Jackson, M. L., 1985, Soil chemical analysis— Advanced course, 2d ed., 11th printing: Madison, Wisconsin, M. Jackson, 895 p.

Katsube, T. J., and M. A. Williamson, 1994, Effects of diagenesis on shale nano-pore structure and implications for sealing capacity: Clay Minerals, v. 29, p. 451–461.

Katsube, T. J., and M. A. Williamson, 1998, Shale petrophysical characteristics: Permeability history of subsiding shales, *in* J. Schieber, W. Zimmerle, and P. Sethi, eds., Shales and mudrocks: II: Stuttgart, Schweizerbart, p. 69–91.

Knipe, R. J., Q. J. Fisher, G. Jones, M. R. Clennell, A. B. Farmer, A. Harrison, B. Kidd, E. McAllister, J. R. Porter, and E. A. White, 1997, Fault seal analysis: Successful methodologies, application and future direction, *in* P. Møller-Pedersen and A. G. Koestler, eds., Hydrocarbon seals. Importance for exploration and production: Amsterdam, Elsevier, p. 15–38.

Koledoye, A. B., A. Aydin, and E. May, 2000, Three-dimensional visualization of normal fault segmentation and its implication for fault growth: The Leading Edge, v. 19, p. 692–701.

Koledoye, B., A. Aydin, and E. May, 2003, A new process-based methodology for analysis of shale smear along normal faults in the Niger Delta: AAPG Bulletin, v. 87, p. 445–463.

Krushin, J. T., 1997, Seal capacity of nonsmectite shale, *in* R. C. Surdam, ed., Seals, traps, and the petroleum system: AAPG Memoir 67, p. 31–47.

Lehner, F. K., and W. F. Pilaar, 1997, The emplacement of clay smears in synsedimentary normal faults: Inferences from field observations near Frechen, Germany, *in* P. Møller-Pedersen

and A. G. Koestler, eds., Hydrocarbon seals. Importance for exploration and production: Amsterdam, Elsevier, p. 39–50.
Lindsay, N. G., F. C. Murphy, J. J. Walsh, and J. Watterson, 1993, Outcrop studies of shale smears on fault surfaces, *in* S. S. Flint and I. D. Bryant, eds., The geological modelling of hydrocarbon reservoirs and outcrop analogues: International Association of Sedimentologists Special Publication 15, p. 113–123.
Manzocchi, T., J. J. Walsh, P. Nell, and G. Yielding, 1999, Fault transmissibility multipliers for flow simulation models: Petroleum Geoscience, v. 5, p. 53–63.
Mesri, G., and R. E. Olson, 1971, Mechanisms controlling the permeability of clays: Clays and Clay Minerals, v. 19, p. 151–158.
Moore, D. M., and R. C. Reynolds, 1997, X-ray diffraction and the identification and analysis of clay minerals: Oxford, Oxford University, 378 p.
Neuzil, C. E., 1994, How permeable are clays and shale?: Water Resources Research, v. 30, p. 145–150.
Pettijohn, F. J., 1975, Sedimentary rocks, 3d ed.: New York, Harper and Row, 628 p.
Pevear, D. R., P. Vrolijk, and F. J. Lomgstaffe [sic], 1997, Timing of Moab fault displacement and fluid movement integrated with burial history using radiogenic and stable isotopes, *in* J. P. Hendry, P. F. Carey, J. Parnell, A. H. Ruffell, and R. H. Worden, eds., Geofluids II '97: Belfast, The Queens University, p. 42–45.
Sakharov, B. A., H. Lindgreen, A. L. Salyn, and V. A. Drits, 1999, Determination of illite-smectite structures using multispecimen XRD profile fitting: Clays and Clay Minerals, v. 47, p. 555–566.
Schowalter, T. T., 1979, Mechanics of secondary hydrocarbon migration and entrapment: AAPG Bulletin, v. 63, p. 723–760.
Skerlec, G. M., 1999, Evaluating top and fault seal, *in* E. A. Beaumont and N. H. Foster, eds., Exploring for oil and gas traps: AAPG Treatise of Petroleum Geology, Handbook of Petroleum Geology, p. 10-1–10-94.
Smith, D. A., 1980, Sealing and non-sealing faults in Louisiana Gulf Coast salt basin: AAPG Bulletin, v. 64, p. 145–172.
Sneider, R. M., J. S. Sneider, G. W. Bolger, and J. W. Neasham, 1997, Comparison of seal capacity determinations: Conventional cores vs. cuttings, *in* R. C. Surdam, ed., Seals, traps, and the petroleum system: AAPG Memoir 67, p. 1–12.
Sperrevik, S., R. B. Faerseth, and R. H. Gabrielsen, 2000, Experiments on clay smear formation along faults: Petroleum Geoscience, v. 6, p. 113–123.
Sperrevik, S., P. A. Gillespie, Q. J. Fisher, T. Halvorsen, and R. J. Knipe, 2002, Empirical estimation of fault rock properties, *in* A. G. Koestler and R. Hunsdale, eds., Hydrocarbon seal quantification: Amsterdam, Elsevier, p. 109–125.
Środoń, J., 1980, Synthesis of mixed-layer kaolinite/smectite: Clays and Clay Minerals, v. 28, p. 419–424.
Środoń, J., V. A. Drits, D. K. McCarty, J. C. C. Hsieh, and D. D. Eberl, 2001, Quantitative x-ray analysis of clay-bearing rocks from random preparations: Clays and Clay Minerals, v. 49, p. 514–528.
Sullivan, R., and J. Waters, 1980, History of Mount Diablo coalfield, Contra Costa County, California: California Geology, v. 33, p. 51–59.
Sullivan, R., J. Waters, and M. D. Sullivan, eds., 1994, Field guide to the geology of Black Diamond Mines Regional Preserve: Northern California Geological Society, 46 p.
Sullivan, M. D., R. Sullivan, and J. Waters, 2003, Reservoir characterization and sequence stratigraphy of the Domengine Formation, Black Diamond Mines Regional Preserve, Northern California. Domengine field trip guidebook: Pacific Section SEPM, 52 p.
Sverdrup, E., J. Helgesen, and J. Vold, 2003, Sealing properties of faults and their influence on water-alternating-gas injection efficiency in the Snorre field, northern North Sea: AAPG Bulletin, v. 87, p. 1437–1458.
van der Zee, W., J. L. Urai, and P. D. Richard, 2003, Lateral clay injection into normal faults: GeoArabia, v. 8, p. 501–522.
Vrolijk, P., and B. A. van der Pluijm, 1999, Clay gouge: Journal of Structural Geology, v. 21, p. 1039–1048.
Watts, N. L., 1987, Theoretical aspects of cap-rock and fault seals for single- and two-phase hydrocarbon columns: Marine and Petroleum Geology, v. 4, p. 274–307.
Weaver, C. E., 1989, Clays, muds, and shales: Amsterdam, Elsevier, 819 p.
Weber, K. J., G. Mandl, W. F. Pilaar, F. Lehner, and R. G. Precious, 1978, The role of faults in hydrocarbon migration and trapping in Nigerian growth fault structures: Society of Petroleum Engineers AIME 10th Annual Offshore Conference Proceedings, v. 4, p. 2643–2653.
Yielding, G., 2002, Shale gouge ratio—Calibration by geohistory, *in* A. G. Koestler and R. Hunsdale, eds., Hydrocarbon seal quantification: Amsterdam, Elsevier, p. 1–15.
Yielding, G., B. Freeman, and D. T. Needham, 1997, Quantitative fault seal prediction: AAPG Bulletin, v. 81, p. 897–917.
Younes, A. I., and A. Aydin, 2001, Comparison of fault sealing by single and multiple layers of shale; outcrop examples from the Gulf of Suez, Egypt (abs.): AAPG Annual Meeting Program, v. 10, p. A222.